Bachelor's Thesis

Simulation of Solar Irradiance During a Total Eclipse

Bachelor's Thesis at the faculty of physics,
Ludwig-Maximilians-University Munich

submitted by
Paul Ockenfuß

Munich, Germany, June 15th 2018

Supervisor:
Prof. Dr. Bernhard Mayer
Dr. Claudia Emde

Bachelorarbeit

Simulation der solaren Bestrahlungsstärke während einer totalen Sonnenfinsternis

Bachelorarbeit an der Fakultät für Physik,
Ludwig-Maximilians-Universität München

vorgelegt von
Paul Ockenfuß

München, den 15. Juni 2018

Betreuer:
Prof. Dr. Bernhard Mayer
Dr. Claudia Emde

Abstract

In this study, a three-dimensional radiative transfer simulation is developed, in order to predict solar irradiance like measured from an earthly observer. Starting from the sun's and moon's position, the programm calculates a realistic profile of the lunar shadow at the top of the atmosphere, including the effect of solar limb darkening. Subsequently, a Monte-Carlo model is used to simulate the transfer of solar radiation through the earth's atmosphere. Among the effects taken into account are the curvature of the earth and various trace gas profiles, as well as the reflectance and elevation of the surrounding area. The model is applied to the total solar eclipse on August 21, 2017 at a position located in Oregon, and to the total solar eclipse on July 2, 2019 like it will be seen from LaSilla Observatory located in Chile. Wavelengths between $300nm$ and $1020nm$ are studied. The influence of the surface reflectance, the ozone profile and mountains surrounding the observer is examined closer. A strongly increased sensivity during totality is found for these parameters, leading to possible changes in irradiance up to a factor 2.0. Using the most realistic guess for each parameter, the model is compared with measurements of the eclipse 2017. During totality, agreement is better than 20% for each wavelength, with less than 10% in the area from $400nm$ to $600nm$.

Contents

Chapter 1

Introduction

Thinking about it, there are not many fundamental sources of energy on earth, despite the vast field of technologies to make them usable. Besides geothermal, nuclear or tidal energy, the by far most important one is the sun. It's the sun's radiation that turns earth from a cold and steady sphere into a vivid planet. The sun is also the motor of all dynamical atmospheric processes. Essentially, it is the unequal distribution of solar radiation at top of atmosphere that causes all global circulations and creates the weather patterns we typically observe. Therefore, a radiative transfer model is a key feature in every advanced weather or climate simulation. The degree of realism in these models depends, among other factors, on the available computational time in every iteration, since radiative transfer can be computationally very expensive. A typical simplification is to use one-dimensional models, where the horizontal characteristics of the atmosphere are assumed to be constant. While they are producing already highly realistic results in many situations, one would expect a fully three dimensional model to be the most general and accurate solution. This is however not easy to proof. Imagine a dessert with a blue sky overhead, no clouds visible anywhere. In this case, it would be an easy task to rebuild the scene in the models and validate them by comparison with radiative measurements, e.g. on the ground. Of course, not much information is gained now, since the initial situation was already "one-dimensional" in matter of radiative transfer. The other extreme would be a cloudy day, with clouds of various different shapes and sizes spread all over the sky. A three dimensional model would be clearly the prefered one here, but the exact virtual reproduction of the scene at the time of the measurement turns out to be an extremly challenging task.

What we would be ideally looking for is a situation in between, with the horizontal conditions variing, but in a precisely controlled manner. This requirement is fulfilled during a total solar eclipse, when the lunar shadow defines the spatial distribution of incident sunlight according to a specific function. Thus, a total solar eclipse represents a great chance to test three dimensional radiative transfer models. In this study, a set of tools to determine the irradiance distribution at top of atmosphere will be developed. They can be used to simulate solar irradiance at the ground with the help of the three dimensional radiative transfer model MYSTIC (Mayer 2009; Emde and Mayer 2007). The tools will be applied to the total solar eclipse 2017 over North America and the influence of several atmospheric and environmental parameters will be analyzed. Furthermore, the outcome will be compared to measurements taken during the eclipse 2017. In the end, an outlook to the total eclipse 2019 will be given, in the hope that this could be used to plan future measurements.

Chapter 2

Theory

2.1 Atmospheric Radiative Transfer

The main objective of radiative transfer in atmospheric science is to calculate the spatio-temporal distribution of deposited energy due to electromagnetic waves. This includes the interaction of light with various atmospheric gases, as well as aerosol particles and cloud droplets in a wavelength range from the ultraviolett up to the microwave region. In the visible part of the spectrum, the most important source of radiation is of course the sun, sending a stream of photons towards the earth. One of the basic assumptions in radiative transfer theory is that the number of photons in an area of interest is always huge enough to neglect the quantization and describe radiation on a macroscopic scale as a continuous stream with some inherent properties like wavelength, direction or polarization.

Looking at this radiative stream in time and space, we can define several quantities of interest shown in Table 2.1. The most important for this study will be Irradiance. It is what we typically measure with a wavelength selective sensor with a certain area. Radiance, on the contrary, only counts the radiation coming from a specific solid angle element $d\Omega = \sin(\theta)d\theta d\phi$. The $\cos(\theta)$ accounts for the lower effective area of the sensor if the angle between incoming radiation and the sensor surface is smaller than 90°. From each of the wavelength dependent quantities we get the wavelength independent counterparts ϕ, E, L, if we integrate over a certain wavelength range $\Delta\lambda$.

Quantity	Symbol	Definition	Unit
Radiant Energy	Q		J
Radiant Power	ϕ_λ	$\frac{dQ}{dt \cdot d\lambda}$	Wnm^{-1}
Irradiance	E_λ	$\frac{dQ}{dA \cdot dt \cdot d\lambda}$	$Wm^{-2}nm^{-1}$
Radiance	L_λ	$\frac{dQ}{dA \cdot \cos(\theta) \cdot d\Omega \cdot dt \cdot d\lambda}$	$Wm^{-2}sterad^{-1}nm^{-1}$

Table 2.1: Important quantities in radiative transfer, given per wavelength. Adapted from Mayer 2009

In the standard scenario, we have knowledge about the optical medium and the radiative field at the boundary, for example the top of atmosphere (TOA). In this case, the radiative transfer equation (RTE, Equation 2.1) tells us how the radiance $L(\mathbf{r}, \mathbf{\Omega}, t)$ evolves depending on the position, the direction and time. In the following, we will look at each of the terms seperately.

$$\frac{1}{c}\frac{\partial L_\lambda}{\partial t} + \mathbf{\Omega} \cdot \nabla L_\lambda = -k_{ext,\lambda} L_\lambda + \frac{k_{scat,\lambda}}{4\pi} \int_{4\pi} P_\lambda(\mathbf{\Omega}', \mathbf{\Omega}) L_\lambda(\mathbf{\Omega}') d\mathbf{\Omega}' + J_\lambda \tag{2.1}$$

2.1.1 Temporal and spatial variation

The first term on the left side of Equation 2.1 describes the temporal variation of the radiance at a fixed position. For most atmospheric applications, it can be neglected. This reflects the fact that a change of the incoming light at TOA almost immediately affects the radiation field everywhere due to the high speed of light c compared to the relevant distances in the atmosphere. The second term $\mathbf{\Omega} \cdot \nabla L_\lambda$ represents the spatial variation in the direction $\mathbf{\Omega}$ at constant time.

2.1.2 Extinction

The negative sign of $-k_{ext,\lambda}L_\lambda$ indicates the extinction of photons from the stream. This does not necessarily mean that the photons are extinct in a physical sense, they can also be outscattered of the direction of interest. Therefore, $k_{ext,\lambda} = k_{scat,\lambda} + k_{abs,\lambda}$. $k_{scat,\lambda}$ and $k_{abs,\lambda}$ are scattering and absorption coefficients. For a medium made out of particles, they can be obtained from the number of constituents per volume n and the respective cross-section per particle σ via $k_\lambda = n\sigma_\lambda$. σ_λ is a measure for the effective statistical area a particle appears to have with reference to a certain kind of interaction and does not always correspond to the real size of it. In the special case where $k_{scat,\lambda} = J_\lambda = 0$ (no scattering or emission inside the medium), there exists an easy solution for the RTE. If we parametrize a straight path $\mathbf{r} = \mathbf{r_0} + s \cdot \mathbf{\Omega}$, introducing the real variable s, we can use a total differential to obtain the left side of the RTE:

$$\frac{dL_\lambda(\mathbf{r}(s), \mathbf{\Omega})}{ds} = \frac{\partial L_\lambda}{\partial x}\Omega_x + \frac{\partial L_\lambda}{\partial y}\Omega_y + \frac{\partial L_\lambda}{\partial z}\Omega_z = \mathbf{\Omega} \cdot \nabla L_\lambda = -k_{abs,\lambda}L_\lambda \tag{2.2}$$

The solution to this equation is just the Lambert-Beer Law with the optical thickness τ defined as $\tau = k_{abs,\lambda}s$:

$$L_\lambda = L_{0,\lambda}e^{-\tau}. \tag{2.3}$$

2.1.3 Absorption

The variation of $\sigma_{abs,\lambda}$ for atoms and molecules usually shows a line pattern, as a result of the discrete nature of quantum mechanics. To get insight into its structure, let's start with a single atom first. The electrons orbiting the nucleus can only be located at discrete energy levels. Photons can be emmitted or absorbed whenever electrons switch between these levels, ensuring that the total energy is conserved. Following $E = h\nu$, one would expcect this process to happen only at specific wavelengths. In reality, there are however several mechanisms that broaden the lines of possible transition wavelengths. The so-called natural line width is independent of the atoms environment and a result of the finite lifetime an electron can be in an excited state. It can be derived analogously to the classical model of a damped osciallator and has a Lorentzian shape (Demtröder 2016, chap. 7.4):

$$I = I_0 \cdot \frac{\gamma/2\pi}{(\omega - \omega_0)^2 + (\gamma/2)^2} \tag{2.4}$$

with I being the intensity of the light emitted or absorbed of the specific transition with frequency ω_0, $\gamma = \frac{1}{\tau}$, τ the average excitation lifetime and $\omega = \frac{2\pi \cdot c}{\lambda}$ the light's frequency. The width of the absorption lines does also depend on the pressure and temperature of the atmospheric layer. In the case of pressure, this can be understood as a reduction of the mean lifetime, as a consequence of the collisions between the atoms, leading to line broadening through the same arguments like for the natural linewidth. The coupling to temperature is simply a result of the Doppler effect. If we assume that the kinetic energy of the individual atoms follows a Boltzmann distribution, with the energy itself being quadratic in the velocity, we can express the number of atoms flying with a certain velocity through the frequency shift of the light we will see from them. Quantitatively (Demtröder 2016, id.),

$$I(\omega) = I_0 \cdot e^{-\left(\frac{\omega-\omega_0}{\delta_{\omega_D}/\sqrt{4\cdot\ln(2)}}\right)^2} \qquad \delta_{\omega_D} = \frac{\omega_0}{c}\sqrt{\frac{8kT\ln(2)}{m}} \tag{2.5}$$

with ω_0 the "rest-frequency", the temperature T, atomic mass m, Boltzmann constant k and c the speed of light. Especially for bigger atoms this already allows a pretty complex structure, despite we only have considered single atoms so far. If two or more atoms form a molecule together, photons can also excite rotational or vibrational modes. Suppose our molecule consists of solely two identical atoms, held together from the potential formed by the mutual combination of their electronic shells. We can reduce the problem to an effective one-body problem introducing relative coordinates. For a constant nuclear distance R, rotational energy eigenvalues can be derived, whereas in the absence of rotation, the potential can be assumed to be quadratic, leading to vibrational eigenvalues:

$$E_{rot} = \frac{\hbar^2 J(J+1)}{2\mu R^2} \qquad E_{vib} = \hbar\omega(\nu + \frac{1}{2}) \tag{2.6}$$

Here, J and ν are rotational and vibrational quantum numbers, μ is the reduced mass of the two nuclei and ω the eigenfrequency of the molecule. Transitions are only possible between states with $\Delta\nu = \Delta J = \pm 1$. Because the energetical jump from $\Delta\nu$ is usually much higher ($10^{-1}eV$ - $10^{-2}eV$, $10\mu m$-$100\mu m$) compared to the one from a change in J ($10^{-4}eV$ - $10^{-5}eV$, $1cm$-$10cm$), this results in a spectra of fine, evenly spaced rotational lines around the vibrational transition.

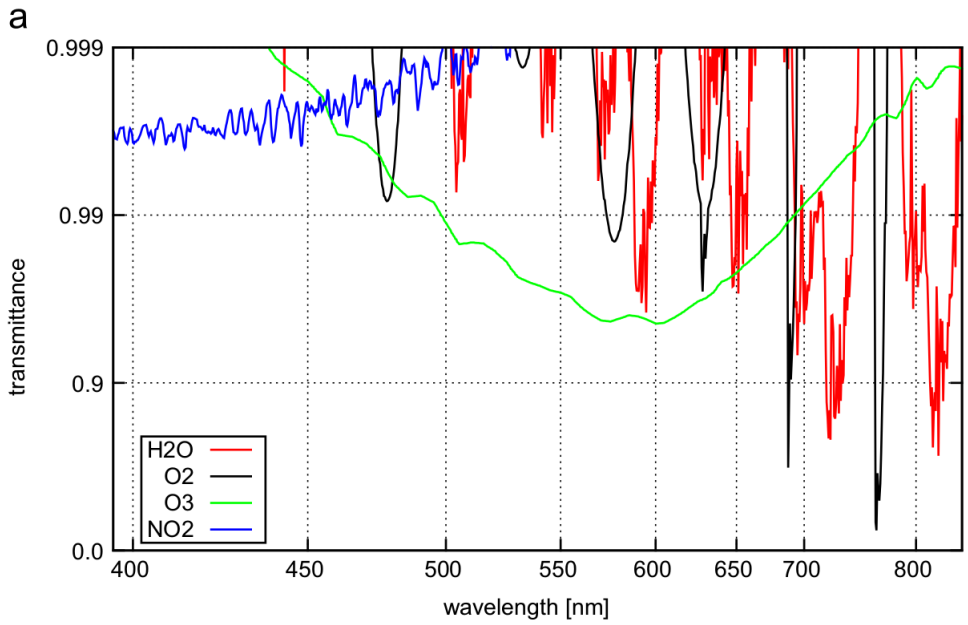

Figure 2.1: Fraction of sunlight coming through the US standard atmosphere (G. Anderson et al. 1986), when only one of the absorption species is set, relative to the transmitted sunlight without trace gases. Taken from Gasteiger et al. 2014.

2.1.4 Scattering

The integral term in the RTE accounts for inscattering of photons, i.e. photons from outside the stream are scattered into the direction of interest. The integral sums up the radiance coming from all directions $\mathbf{\Omega}'$ weighted with the so called phase function $P_\lambda(\mathbf{\Omega}', \mathbf{\Omega})$. It gives us the probability for scattering from direction $\mathbf{\Omega}'$ to $\mathbf{\Omega}$, assumed we already know that a scattering event takes place. Therefore, the phase function fulfills the normalization condition

$$\frac{1}{4\pi}\int_{4\pi} P_\lambda(\mathbf{\Omega}', \mathbf{\Omega}) d\mathbf{\Omega}' = 1 \tag{2.7}$$

The probability that scattering happens at first instance is again included in the prefactor $k_{scat,\lambda}$. Depending on the ratio of wavelength and scattering particle size, one generally distinguishes three scattering types: For particles much smaller than the wavelength, Rayleigh scattering takes place. In the limit of very large particles, we can use the geometrical optics formulas and describe electromagnetic waves as rays, which are reflected are absorbed.

For medium sized particles, one approach would be the so-called Mie-theory, which applies Maxwell's relations to spherical particles.The following provides a brief summary of the complete derivation in Zdunkowski et al. 2007. We start with the Maxwell equations in matter, which read

$$\nabla \times \mathbf{E} + \frac{\partial \mathbf{B}}{\partial t} = 0 \qquad \nabla \times \mathbf{H} - \frac{\partial \mathbf{D}}{\partial t} - \mathbf{J} = 0 \tag{2.8}$$

with $\mathbf{J} = \sigma\mathbf{E}$, $\mathbf{D} = \epsilon\mathbf{E}$, $\mathbf{H} = \mathbf{B}/\mu$, where $\mathbf{E}$ and $\mathbf{B}$ are electric and magnetic fields, $\epsilon_{(0)}$ and $\mu_{(0)}$ are permittivity and permeability (of free space) and σ the electrical conductivity. For the incoming fields $\mathbf{E}$ and $\mathbf{B}$, the ansatz of a plane wave in a cartesian coordinate system with the origin located in the center of the spherical particle, travelling in z-direction with wave number k_0 and frequency ω, is made:

$$\mathbf{E}^i = \mathbf{e}_x E_0^i e^{i(k_0 z - \omega t)} \qquad \mathbf{H}^i = \mathbf{e}_y H_0^i e^{i(k_0 z - \omega t)} \tag{2.9}$$

$\mathbf{e}_x$ and $\mathbf{e}_y$ are the arbitrarily oriented unit vectors of the cartesian coordinate system. The basic idea in Mie's approach is that Equation 2.9 can also be expressed in spherical coordinates (r, θ, ϕ), if we allow a series expansion. The final results of the longer calculations are

$$\mathbf{E}^i = E_0^i \sum_{n=0}^{\infty} (\mathbf{M}_{v_n^i} - i\mathbf{N}_{u_n^i}) \qquad \mathbf{H}^i = H_0^i \sum_{n=0}^{\infty} (\mathbf{M}_{u_n^i} + i\mathbf{N}_{v_n^i}) \qquad H_0^i = \sqrt{\frac{\epsilon_0}{\mu_0}} E_0^i \tag{2.10}$$

$$\mathbf{M}_{\Psi_n} = \nabla \times (\mathbf{r}\Psi_n) \qquad \mathbf{N}_{\Psi_n} = \frac{1}{k_0}\nabla \times \mathbf{M}_{\Psi_n} \tag{2.11}$$

$$u_n^i = i^n \frac{2n+1}{n(n+1)} \cos(\phi) P_n^1(\cos(\theta)) j_n(k_0 r) e^{-i\omega t} \qquad v_n^i = i^n \frac{2n+1}{n(n+1)} \sin(\phi) P_n^1(\cos(\theta)) j_n(k_0 r) e^{-i\omega t} \tag{2.12}$$

Here, $P_n^m(x)$ are so-called associated Legendre polynomials and $j_n(x)$ spherical Bessel functions of the first kind. Now, suppose the incident wave arrives at a boundary level of a medium, where the permittivity and permeability undergo a sudden change. In this case, we declare two new electric and magnetic fields $\mathbf{E}^{t,s}$ and $\mathbf{H}^{t,s}$, with t denoting the transmitted quantities inside the medium and s the scattered waves outside. We can make a series approach similar to Equation 2.10 for them, with some slight differences. The missing knowlegde in the amplitude of the transmitted and scattered waves is expressed in unknown prefactors $a_n^{t,s}$ and $b_n^{t,s}$ in front of the expressions in Equation 2.12, and, due to arithmetic issues, the Bessel functions in the scattering terms are replaced by spherical Hankel functions of the first kind.

So far, only mathematical transformations were applied to general solutions of the Maxwell equations in homogenous media. To determine the unknown prefactors, the scattered and transmitted waves are related to the incoming one via boundary conditions for the surface-parallel component of the electric and magnetic field. They read

$$\mathbf{n} \times (\mathbf{E_2} - \mathbf{E_1}) = 0 \qquad \mathbf{n} \times (\mathbf{H_2} - \mathbf{H_1}) = 0 \tag{2.13}$$

with $\mathbf{n}$ the surface normal of the boundary layer, $\mathbf{E}_1$, $\mathbf{H}_1$ electric and magnetic field evaluated directly above the layer and $\mathbf{E}_2$, $\mathbf{H}_2$ evaluated directly below. In our case, $\mathbf{E}_2 = \mathbf{E}^i + \mathbf{E}^s$, $\mathbf{E}_1 = \mathbf{E}^t$ ($\mathbf{H}$ analog) and $\mathbf{n} = \mathbf{e}_r$, where the assumption of a spherical particle located at the origin comes in with the last relation. This allows the derivation of expressions for $a_n^{t,s}$ and $b_n^{t,s}$, and finally for an analytical expression of the transmitted and scattered electric and magnetic fields. In the Rayleigh limit, i.e. in the case of a sphere with a small radius a, compared to the incident wavelength λ, the electric field takes a compact form, namely:

$$\begin{pmatrix} E_\theta^s \\ E_\phi^s \end{pmatrix} = \frac{4\pi^2 a^3}{\lambda^2 r} \frac{N^2-1}{N^2+2} e^{ik_0(r-z)} \begin{pmatrix} \cos(\theta) & 0 \\ 0 & 1 \end{pmatrix} \begin{pmatrix} E_l^i \\ E_r^i \end{pmatrix} \tag{2.14}$$

N is the (complex) index of refraction inside the medium. The incident electric field is given in a cartesian coordinate system (l, r), rotated counterclockwise by ϕ relative to the original x, y system. Figure 2.2 gives an overview of the coordinate systems used here. The important thing to mention at this point is the λ^{-2} dependence of the scattered field. Radiance, which is the squared norm of the field vector, therefore goes like λ^{-4}.

In order to derive the phase function from Mie theory, we have to define the scattered flux Φ^s, which is the total radiance due to scattering, summed over a spherical surface around the particle. Radiance in turn is equal to the square of the amplitude of the electric field.

$$\Phi^s = \int_{4\pi r^2} L^s dA \qquad L^s = \alpha(\cos(\theta)^2 + 1) L^i \tag{2.15}$$

Here, we absorbed all prefactors independent of θ, ϕ in α. For the phase function, we look at the change of this flux with solid angle, normed to the incoming flux densitiy and a small volume element. To fulfill the condition in Equation 2.7, a second normalization over solid angle is applied.

$$P(\cos(\theta)) = \frac{4\pi \tilde{P}(\cos(\theta))}{\int_{4\pi} \tilde{P}(\cos(\theta)) d\Omega} \qquad \tilde{P}(\cos(\theta)) = \frac{d\Phi^s(\cos(\theta))}{\delta V d\Omega dL^i} \tag{2.16}$$

To obtain the Rayleigh phase function, we apply Equation 2.16 to Equation 2.14. With the use of

$$\frac{d\Phi^s}{d\Omega} = r^2 \frac{d\Phi^s}{dA} = r^2 dL^s \tag{2.17}$$

, the prefactors cancel out, so we can perform the angle normalization and finally obtain

$$P_{Ray}(\cos(\theta)) = \frac{3}{4}(1 + \cos^2(\theta)) \tag{2.18}$$

In Figure 2.3, we can see the phase function plotted for particles of different sizes. For very small particles (dashed line), the Rayleigh limit is approached, where scattering in the forward and backward hemisphere is equally likely. For increasing size parameters, the forward directions take over, with an extremly large peak in the direction of incidence, and the structure becomes more complex in general.

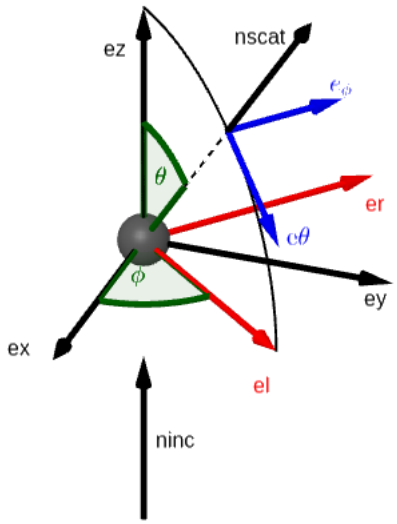

Figure 2.2: Coordinate systems used in Mie theory. The spherical particle is located in the origin. "l" and "r" refer to "parallel" and "perpendicular" to the scattering plane, that is the plane spanned by the incoming and scattered propagation vectors.

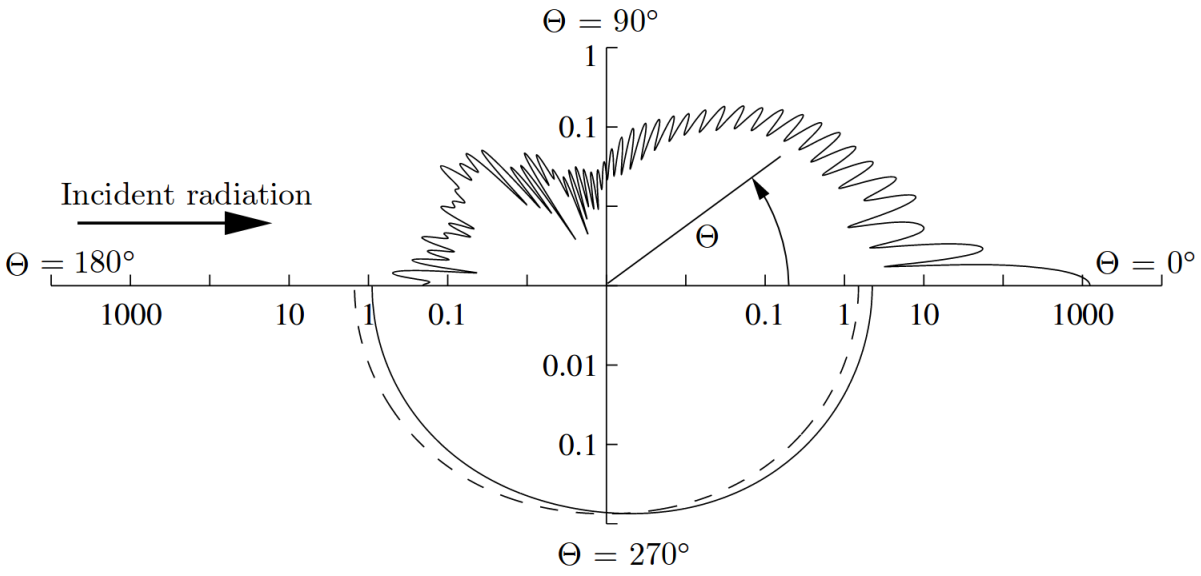

Figure 2.3: Polar plot of $P(\cos(\theta))$ calculated using Mie theory with $N = 1.33 + 0i$ (corresponds to water) and three different size parameters $x = 2\pi r/\lambda$. Dashed curve: $x = 0.01$, lower solid curve: $x = 1$, upper solid curve: $x = 50$. The phase functions are symmetric with respect to the axis of incidence, the distinction between the curves in the upper half of the plot and the cuves in the lower half is made only for better visibility. Picture taken from Zdunkowski et al. 2007, p. 367.

2.1.5 Albedo

Another important kind of scattering for radiative transfer applications, that has to be mentioned at this point, is the reflection of light at the earth's surface. Generally, we observe different behaviour for different materials when radiated with light. They appear to have different colors as a consequence of their tendency to reflect some wavelengths more than others, they can appear brighter or darker depending on the amount of radiation reflected back to the observer, and they have the quality we might call "shininess", describing wether light is reflected diffuse or more focused, like e.g. from a mirror. The most important quantity for this study is the surface albedo, defined as the ratio of the scattered irradiance E_s and the incoming irradiance E_r.

$$A = \frac{E_s}{E_i} \tag{2.19}$$

It is important to mention that the albedo is not a completely inherent property of the surface, but also depends on the angle of the incoming solar radiation. The information about the distribution of the outgoing radiation is not contained in the albedo. In the special case of equal radiance L in every direction, the term *Lambertian albedo* is used. A surface with Lambertian albedo appears equally bright regardless of the angle from which it is observed. Examples for different materials are given in Figure 2.4.

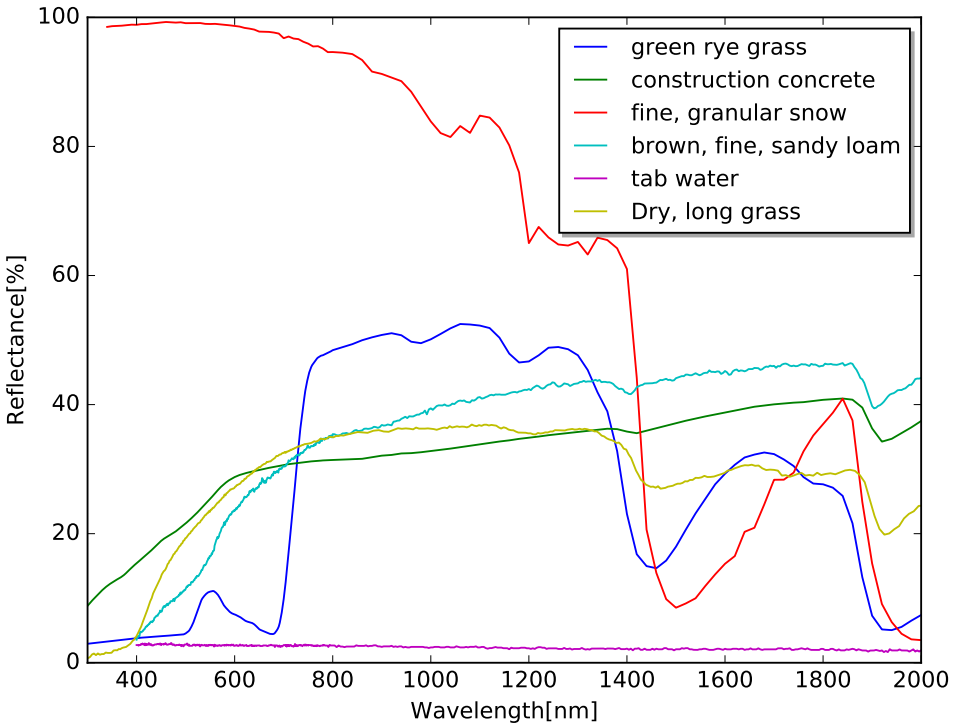

Figure 2.4: Albedo for different materials, in %. We see that the full range of possible values could be encountered for everyday materials which are also common on the earth's surface. Whereas certain kinds of snow are able to reflect nearly all visible light, water appears essentially black (The blueness of the oceans is actually the reflection of the sky in the water). The sudden jump around $700nm$ for green grass is typical for most kinds of green vegetation. Data from *ECOSTRESS spectral library* 2018

2.1.6 Sources of radiation

In order to do radiative transfer with use of the RTE, we need of course a source of radiation at first. In the ultraviolett and visible range, the only natural source of radiation is the sun. Its spectrum is close to that of a black body with the same temperature as the average surface temperature of the sun of approximately 5778K. The formula for the radiance of a black body, depending on wavelength λ and temperature T reads:

$$L_\lambda = \frac{2 \cdot h \cdot c^2}{\lambda^5} \cdot \frac{1}{e^{\frac{h \cdot c}{\lambda \cdot k \cdot T}} - 1} \tag{2.20}$$

Here, h is Planck's constant, c the speed of light and k the Boltzmann constant. Values calculated with Equation 2.20 have to be integrated over half space to get the irradiance emitted from a surface, yielding a factor π. To obtain the solar spectrum at TOA,we need to further correct the result for the earth-sun distance R_{SE}. The radiation from the sun emerges from the surface of a sphere with the sun's radius R_S and is distributed over an area of $4\pi r^2$ in a distance r. Therefore, we have

$$E_{\lambda,Earth} = \frac{R_S^2}{R_{SE}^2}\pi L_\lambda(5778K) \tag{2.21}$$

as a first approximation for the irradiance at TOA, shown as the red curve in Figure 2.5. An important difference are the Fraunhofer-Lines, where the absorption of several elements in the sun's atmosphere create sharp dips in the solar spectrum. In Figure 2.5, some of these lines are clearly visible, e.g. from iron ($382nm$) and Ca^+ ($393nm$).

A second source of radiation could be the optical medium itself. The term J_λ represents emission into direction $\mathbf{\Omega}$. In the atmosphere, we normally have Planck radiation coming from temperatures around 288K, resulting in infrared radiation mainly between $4\mu m$ and $50\mu m$ with a peak at around $10\mu m$. Since the overlap between solar and thermal emission is small, we have the possibility to treat solar and thermal radiative transfer seperately with $J_\lambda(\mathbf{r}, \mathbf{\Omega}) = 0$ in the solar part.

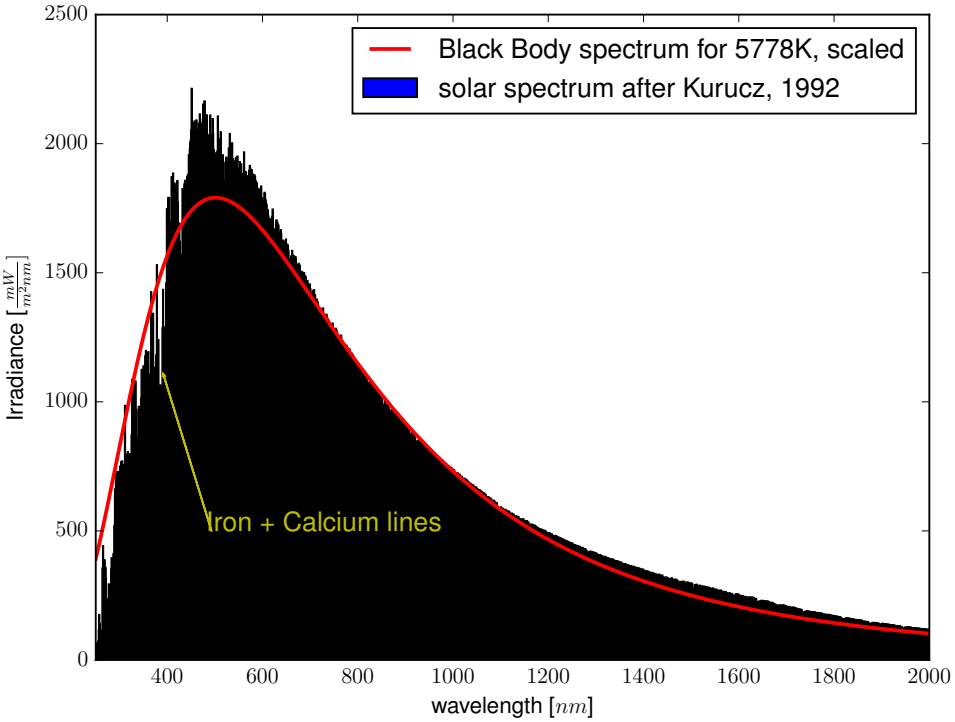

Figure 2.5: Solar irradiance for different wavelengths at TOA. Data after Kurucz 1992, averaged over steps of $1nm$. The red line describes the emission spectrum of a black body at 5778K, corrected for the sun-earth distance.

2.2 Solving the RTE

Besides some special examples like the beforehand mentioned Lambert-Beer law, there exists no general analytical solution for the RTE, especially not for the complex media and phase functions in real world. There are several numerical approximations to calculate radiance distributions, most of them apply only to one-dimensional models, where the atmosphere is assumed to be homogenous in horizontal direction (x,y) and varies only in the vertical (z). Whenever one-dimensional calculations are performed, the RTE could be solved using an implementation of the so-called discrete ordinate method like it was described in Stamnes et al. 1988. The basic idea behind this approach is to use series expansions as approximations: Legendre polynomials in the case of the phase function and Fourier summands for the radiance's azimuth dependence. A further discretization is applied to the elevation angle, leading to a system of coupled, linear, inhomogenous differential equations, which can be solved with an eigenvalue approach like it is common for these systems.

2.2.1 Monte Carlo Models

A horizontally homogenous atmosphere is not always a reasonable assumption, like a short glance in the sky on a cloudy day confirms. Often we have areas of clear sky in between of clouds with complicated shapes. A method to calculate radiative fluxes in nearly arbitrarily complex setups are statistical simulations like Monte Carlo models. They provide a rather intuitive approach close to the physical principles the RTE is based on. Individual photons are started at TOA and their path is traced through the atmosphere until they are absorbed or leave on the top again. To simulate a different path for every photon, random numbers are used. For example, if a photon is scattered on an oxygen molecule, a random number according to the Rayleigh phase function is drawn to determine its new direction. This seems pretty straightforward, however the underlying mathematical proofs are not always trivial. Who guarantees that these models formally solve the RTE and lead to the same results as non-statistical methods? In the following, some basic steps to set up a Monte Carlo model are presented, together with some motivations why this might work. The basis for this part are Mayer 2009 and Marshak et al. 2005.

The first step is the production of samples x_i from a random variable x with a certain distribution function $p(x)$. On computers, there exist several algorithms that can produce so-called pseudo-random numbers, which are typically equally distributed. Now suppose we have one of these random numbers r e.g. between 0 and 1. If we now want to use r to draw one of six categories $A_i, i \in \{1, ..., 6\}$ with a corresponding probability P_i, the easiest way would be to divide the interval into boxes of size P_i and look in which box r will "fall". The number i of this box is therefore determined by

$$\sum_{k=1}^{i} P_k \leq r < \sum_{k=1}^{i+1} P_k \tag{2.22}$$

If we increase the number of boxes more and more while reducing the probability for each box, we can neglect the difference between both sums and write them as an integral

$$r \approx \int_0^x P(k)dk = F(x). \tag{2.23}$$

Taking the inverse $F^{-1}(r) = x$, we have the desired relationship to produce P-distributed random numbers x from r.

Now we can use these numbers together with what is known as the weak law of large numbers in probability theory. It states that the average of samples from a random variable comes infinitely close to the true expectation value of the variable, if we take enough samples. This is still true if we plug our random variable x into a function ϕ (you can think of ϕ as a new random variable itself if you want), so we can approximate the expectation value E_ϕ, defined by an integral over P and ϕ, with the average of our samples:

$$E_\phi = \int P(x)\phi(x)dx \approx \frac{1}{N}\sum_{i=1}^{N} \phi(x_i) \tag{2.24}$$

This equation is the central statement of Monte Carlo estimations. It allows us to convert the integral on the left side to a sum, assumed we know how to integrate P alone to produce the random samples. For example, we can now calculate the transmission of a non-scattering atmosphere with only absorption and thickness s_A. Our intuitive approach would maybe be to start photons at TOA vertically downward and draw random numbers s, according to Lambert-Beer's law, between 0 and ∞ to decide how far they will travel. At the end, we count all photons hitting the ground and compare their number to the total number of photons. Formally, we can do this by introducing the indicator function

$$\phi(s) = \begin{cases} 1 \text{ if } s \geq s_A \\ 0 \text{ if } s < s_A \end{cases} \tag{2.25}$$

Equation 2.24 then proofs that counting photons this way leads to the same result for transmission as evaluating the Lambert-Beer Law at the surface and dividing by the initial radiation L_0 directly:

$$\frac{\sum_{i=1}^{N_{tot}} \phi(s_i)}{N_{tot}} = \int_{s_A}^{\infty} e^{-k_{abs,\lambda}s} \cdot 1ds = -e^{-k_{abs,\lambda}\infty} + e^{-k_{abs,\lambda}s_A} = \frac{L_\lambda(s_A)}{L_{0,\lambda}} \tag{2.26}$$

Essentially, we can use this concept to simulate most of the important aspects of radiative transfer. After we have selected the optical thickness the photon can traverse undisturbed, we use a second random number to decide which type of interaction will happen (cloud scattering, Rayleigh scattering, absorption,...). In case of scattering, we select the new direction from the appropriate phase function with the help of a third random number and let the photon continue its way. Surface reflection can be included in a similar manner.

The Achilles' heel of Monte Carlo estimations hides already in the basic Equation 2.24. The approximation is only valid for a large amount of samples N, but how large is large enough? Let's start with a random variable ϕ with expectaition value E_ϕ and variance D_ϕ again. Dividing ϕ by a natural number N, considering the arithmetic of random variables, results in new values $\frac{E_\phi}{N}$ and $\frac{D_\phi}{N^2}$. At this point, we can apply the central limit theorem, one of the key sentences in probability theory. It states that if we sum N not necessarily normally distributed samples from a random variable x, the sum itself is normally distributed with expectation value NE_x and variance ND_x. Therefore, the sum on the right side of Equation 2.24 is normally distributed with expectation value $N\frac{E_\phi}{N} = E_\phi$ and variance $N\frac{D_\phi}{N^2} = \frac{D_\phi}{N}$. If we now want to know the probability P for the approximation in Equation 2.24 to hold up to a deviation of $c\sqrt{\frac{D_\phi}{N}}$, that is

$$P(c) = Prob\left\{\left|E_\phi - \sum_{i=1}^{N}\frac{\phi_i}{N}\right| < c\sqrt{\frac{D_\phi}{N}}\right\}, \tag{2.27}$$

we have to integrate the normal distribution over the appropriate interval:

$$P(c) = \int_{E_\phi - c\sqrt{\frac{D_\phi}{N}}}^{E_\phi + c\sqrt{\frac{D_\phi}{N}}} \frac{1}{\sqrt{2\pi D_\phi/N}} e^{-\frac{(x-E_\phi)^2}{2D_\phi/N}} dx = \frac{2}{\sqrt{2\pi}}\int_0^c e^{-\frac{t^2}{2}} dt \tag{2.28}$$

c is an arbitrary real parameter in this case. In the second equality, we integrated by substitution and used the fact that the resulting function is symmetric. To obtain a good Monte Carlo approximation with only a few samples N, we would have to use small c in equation Equation 2.27, but following Equation 2.28, this would go along with a small probability to occur. The only way to get good results in almost every run is to use enough samples N compared to the variance D_ϕ of every sample.

This turns out to be problematic when calculating very rare events. Take for example a small, narrow sensor standing on a giant field. The probability p for a photon to hit the sensor would be extremly small compared to the probability $1-p$ to hit the field somewhere else. Of course, this is also true for the variance $D = p - p^2$, but normally we are not interested in results with a small absolute fluctuation (e.g. $1\frac{W}{nm\cdot str}$), but rather in results with a high relative accuracy (e.g. less than 5% deviation from the true value of $0.01\frac{W}{nm\cdot str}$). This means we want Equation 2.29 to be true which is more difficult the smaller p becomes:

$$\frac{c\sqrt{D/N}}{E} = c\sqrt{\frac{1-p}{Np}} \overset{!}{<<} 1 \tag{2.29}$$

In order to get good results in these cases, people came up with a whole bunch of tricks to speed up calculations, known as variance reduction techniques. One example also used in MYSTIC is the replacement of absorption by photon weights. This means that every photon gets equiped with an initial weight of one. The only possible interaction of a photon will be scattering from now on, i.e. $k_{ext,\lambda} = k_{scat,\lambda}$. Whenever a point of interaction is determined, the photon's weight is multiplied by the probability that it had reached this point without gotten absorbed. If the surface is treated as a mixture of absorption (albedo) and scattering (e.g. lambertian), every photon is theoretically traced until it leaves the atmosphere on top. If on this way the photon hits a point we are interested in, the photon's weight is added to the counter. In the end, this leads to more photons contributing (less) to the result.

However, the problem that very rare events almost never occur remains. A solution is provided by the so-called local-estimate technique. A mathematical derivation can be found in Marshak et al. 2005. Basically, it is an analytical estimation of the probability that the photon would reach the sensor directly from it's current position. Whenever scattering happens, we caluculate a new photon direction as always, but moreover, we also calculate the probability that the photon *would* have been scattered into the direction of the sensor and reached it without further interaction. The weight the photon would have had in this case is counted. This allows us to ensure that every photon contributes a (very small) amount to the result. Basically, the idea of both steps is to use the fact that we already know the probability distribution of some of the subprocesses in our model exactly, getting us faster to results we would otherwise need many more iterations to obtain.

Chapter 3

Methods and Techniques

The basis of this work were the calculations done by Emde and Mayer 2007 for the simulation of the total solar eclipse on March 29, 2006. Their program files were written to match the exact conditions at the measurement site 2006, so the simulation code had to be generalized. This includes the possibility to simulate fluxes on positions not directly at the shadow's center line, as well as the adaption to different celestial parameters like the apparent radius of sun and moon or the exact shape of the shadow on the earth. There was also the need to gather new sources of celestial input data, because some of the files used in 2006 were not available anymore in this form in 2017. The overall philosophy was to keep the program as flexible as possible to allow simulations of upcoming solar eclipses at arbitrary observer positions on the globe. The languages used were python for processing of in- and output data and C for the calculations itself.

The whole simulation process can be divided into two parts like it is shown in Figure 3.1. Everything below the sampling plane belongs to the atmospheric part of the simulation. Here, everything concerning the earth and the atmosphere is handled, e.g. absorption by (trace) gases, scattering of molecules and clouds or the spherical geometry of the earth. This part does not "know" anything about the eclipse. It will result in the so-called contribution function C, which gives us the contribution of every point in the sampling plane to the (ir-)radiance at the observer position under the assumption of homogenous illumination in the sampling plane.

The solar eclipse comes in with the celestial part, that is the upper half of Figure 3.1 above the sampling plane. It deals with the solar limb darkening and the planetary positions of sun and moon to calculate the actual radiance distribution in the sampling plane.

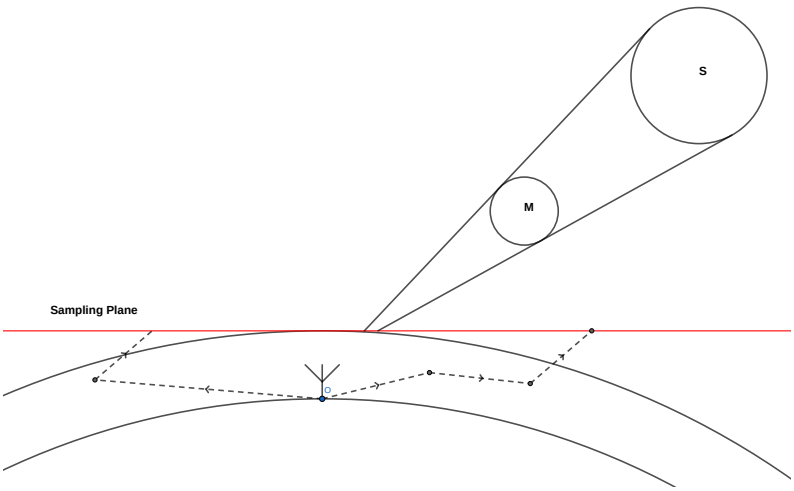

Figure 3.1: Schematic illustration of a solar eclipse and definition of the sampling plane. S denotes the sun, M the moon and O the observer. The dashed lines show simple exemplary photon paths. In the atmospheric part, the solar angle is assumed to be constant.

3.1 Celestial Part

3.1.1 Sources of Planetary Data

There were two main sources of planetary and eclipse data for the simulations. Fred Espenak from Goddard Space Flight Center provides a lot of information around solar eclipses. A part of it is available via the NASA's eclipse website (Young 2018), whereas nearly all kind of parameters can be found in his solar eclipse bulletins, for example Espenak and J. Anderson 2004. Here especially the path tables for the solar eclipses 2006 and 2017 are of importance which provide the time resolved position of the moon's shadow on the earth's surface. Together with the length of the semiminor axis of the elliptical shadow, taken from table four of Espenak and J. Anderson 2004, Emde and Mayer 2007 developed a way to calculate the spatial irradiance distribution in the sampling plane. Their calculation therefore works without knowledge of direct planetary parameters like the solar/lunar radius or distances, but this comes along with some disadvantages when calculating irradiance time series over a longer time interval (e.g. 1+ hours). For example, it is possible for a solar eclipse to take place in the morning during sunrise like it is the case for the eclipse 2017 at positions in the western US. In this case, the irradiance at the surface might already be influenced by the penumbral shadow, while the umbral shadow still "misses" the earth like it is illustrated in Figure 3.2. Consequently there is no path data available for this time. On longer time scales, the assumption of linearity of some parameters might also not be perferct any more.

To avoid these problems and increase flexibility, *JPL Horizons On-Line Ephemeris System* 2018 was used as the second source for celestial data. The service provides access to the JPL Horizons system operated by the Solar System and Dynamics Group of the Jet Propulsion Laboratory (JPL). It offers the possibility to create ephemeris for various celestial bodies in the solar system for arbitrary observer positions on earth. Easy and quick access can be gained by a web interface. To ensure reproducibility, in our case all requests were made using the provided perl script to read in the configuration files and send them to Horizons. A python wrapper was written to automatically modify these configurations if necessary. The most important categories used were azimuth, elevation, apparent angle diameter and distance from observer (categories 4,13,21) respectively for sun and moon (ID 10 and 301). These quantities can be interpreted as spherical coordinates of sun and moon in a local coordinate system centered at the observer. From there, we can derive all further quantities of interest.

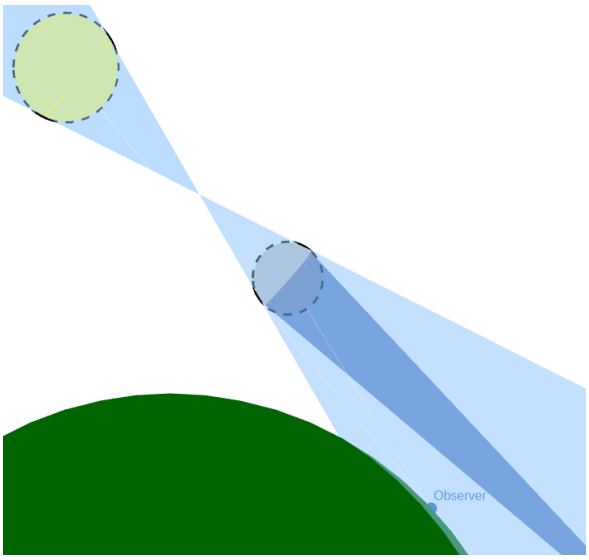

Figure 3.2: Even if the umbral shadow of the moon misses the earth, a partial solar eclipse can be observed in the region of the penumbral shadow.

3.1.2 Solar Irradiance Distribution

The calculation of solar irradiance at a given position and time was done following the geometrical considerations in Koepke et al. 2001. Basically, they integrate over the visible part of the solar disk, weighted with a function that expresses solar limb darkening, described in more detail in subsection 3.1.3. For this and all further calculations, apparent celestial distances are always measured in apparent radii of the sun R_S (note that this is different from Koepke et al. 2001, where the sum of solar and lunar apparent radius $R_M + R_S$ is taken as normalization). R_S in turn is given as an angle, which describes the width of the solar disk in *deg*

or *rad*, see Figure 3.3b. Solar and lunar disk are assumed to be perfect circles, so the problem reduces to the determination of the visible area of a circle with radius one, covered by a circle with radius $\rho = R_M/R_S$ and the centers separated by a distance X. The information about the size and position of the shadow is contained in the spatial variation of X and ρ in the sampling plane.

In order to get the apparent angle X at arbitrary positions $\mathbf{d}$ relative to the observer, we just have to calculate the angle between the position vectors of Sun and Moon as seen from $\mathbf{d}$. We obtain:

$$X(\mathbf{d}, t) = \arccos\left(\frac{(\mathbf{P_S} - \mathbf{d}) \cdot (\mathbf{P_M} - \mathbf{d})}{|\mathbf{P_S} - \mathbf{d}|\,|\mathbf{P_M} - \mathbf{d}|}\right) \tag{3.1}$$

with $\mathbf{P_S(t)}$ and $\mathbf{P_M(t)}$ the position vectors of sun and moon relative to the observer at time t. Assumed that we already have the elevation and azimuth angle of sun and moon like seen from the position $\mathbf{d}$, we can derive a formula to direclty calculate X from these angles: Expressing $\mathbf{P_S} - \mathbf{d}$ and $\mathbf{P_M} - \mathbf{d}$ through $\theta_{M,\mathbf{d}}$,$\phi_{M,\mathbf{d}}$ and $\theta_{S,\mathbf{d}}$,$\phi_{S,\mathbf{d}}$ in their cartesian form, we can evaluate the scalar product in Equation 3.1 and simplify it under use of a trigonometric addition theorem to obtain

$$X(\theta_{M,\mathbf{d}}, \phi_{M,\mathbf{d}}, \theta_{S,\mathbf{d}}, \phi_{S,\mathbf{d}}) = \arccos(cos(\theta_{M,\mathbf{d}}) \cdot cos(\theta_{S,\mathbf{d}}) \cdot cos(\phi_{S,\mathbf{d}} - \phi_{M,\mathbf{d}}) + sin(\theta_{M,\mathbf{d}}) \cdot sin(\theta_{S,\mathbf{d}})) \tag{3.2}$$

The elevation θ is measured from the surface in this expression. Equation 3.2 is used to calculate X at the observer position, where the angles are given directly from the JPL data.

While the spatial variation of the sun-moon distance X is the key quantity for the description of the eclipse, the variation of $\rho(\mathbf{d}, t)$ provides only a small correction. An expression can be derived from the geometry shown in Figure 3.3b with the distance $|\mathbf{P_M} - \mathbf{d}|$ of the moon and the actual lunar radius which was set to $Rad_M = 1737.4km$ (*NASA Moon Fact Sheet* 2018).

$$R_M(\mathbf{d}, t) = \arcsin\left(\frac{Rad_M}{|\mathbf{P_M} - \mathbf{d}|}\right) \tag{3.3}$$

The time evolution of R_M at different places is shown in Figure 3.4. There are two calculations where Equation 3.3 was used, one directly at the observer position and one at a point located on the earth's surface, $500km$ away into the sun's azimuth direction. The third line is the lunar radius at the observer obtained directly from JPL Horizons. The excellent agreement of the two observer calculations validates Equation 3.3, whereas the calculation $500km$ away reveals that there is indeed a small change in the apparent angular lunar radius. For the sun however, a similar calculation shows that the relative change of the apparent radius due to movements in the sampling plane is of the order 10^{-6} because of the much greater distance to the earth, so it is safe to set $R_S(\mathbf{d}, t) = R_S(t)$. In a $2000km$ x $2000km$ sampling plane, the ratio ρ of the radii varies from one end to the other at the time of totality (17:20) from 1.02531 to 1.02948.

The straightforward implementation to get the irradiance at the observer would be to weight every sample bin in the contribution function C with the relative solar irradiance $w(X, \rho, \lambda)$, evaluated at the appropriate position and time in the sampling plane. However, every one of these evaluations requires an integration of the visible part of the solar disk. If we would use 5000 supporting points for the numerical integration, we would end up for a 2000 x 2000 contribution function with at least $2 \cdot 10^{10}$ necessary calculations, which is too much to produce time series in a reasonable calculation time. Fortunately, this is not necessary because of the elliptical symmetry of the lunar shadow at TOA as well as the smooth gradient of $w(X, \rho, \lambda)$, so it is possible to precalculate w for different X and ρ and use these samples to weight the contribution function. For X, there were used 4000 equidistant sampling points. ρ was sampled at 9 different values which are not equidistant. They are choosen automatically by the program, which estimates the value of ρ at certain distances from the observer, for the solar eclipse at hand. Most of these distances are set corresponding to positions centered closer around the sunspot in the sampling plane. This is driven by the fact, that during totality, when the lunar umbral shadow covers the point of direct incident sunlight, most of the diffuse scattered photons are coming from regions not to far away from the umbral shadow. In Figure 3.5, $w(X, \rho, \lambda)$ is shown for $\lambda = 555nm$ at time 17:20.

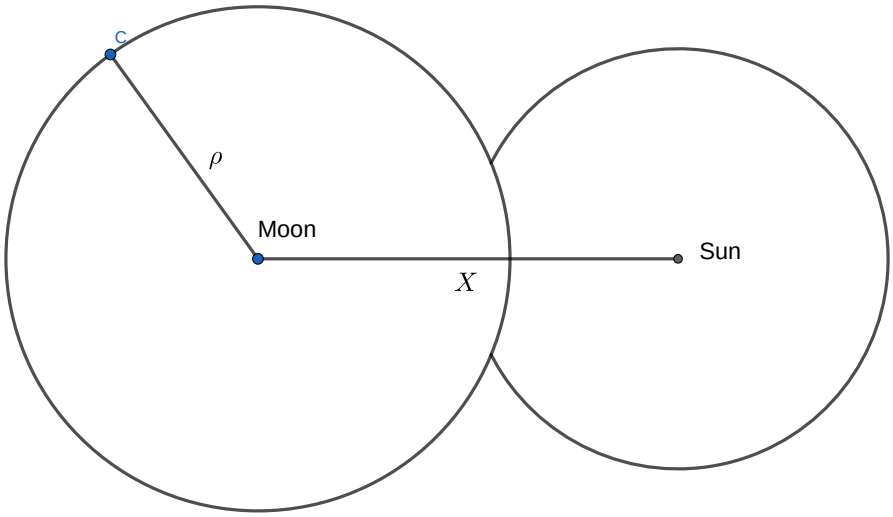

(a) Geometry in analogy to Koepke et al. 2001 like it is seen from an earthly observer.

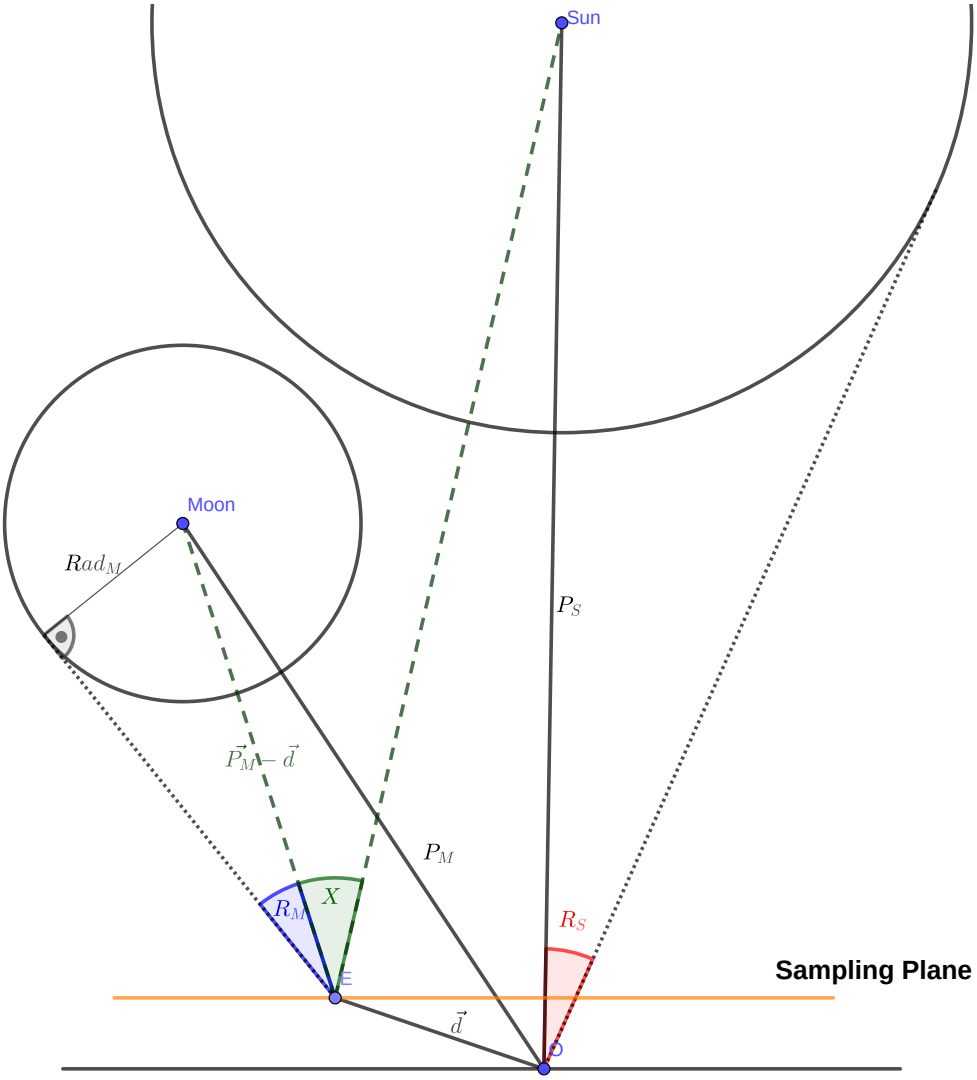

(b) The same situation like in (a), seen from the side.

Figure 3.3

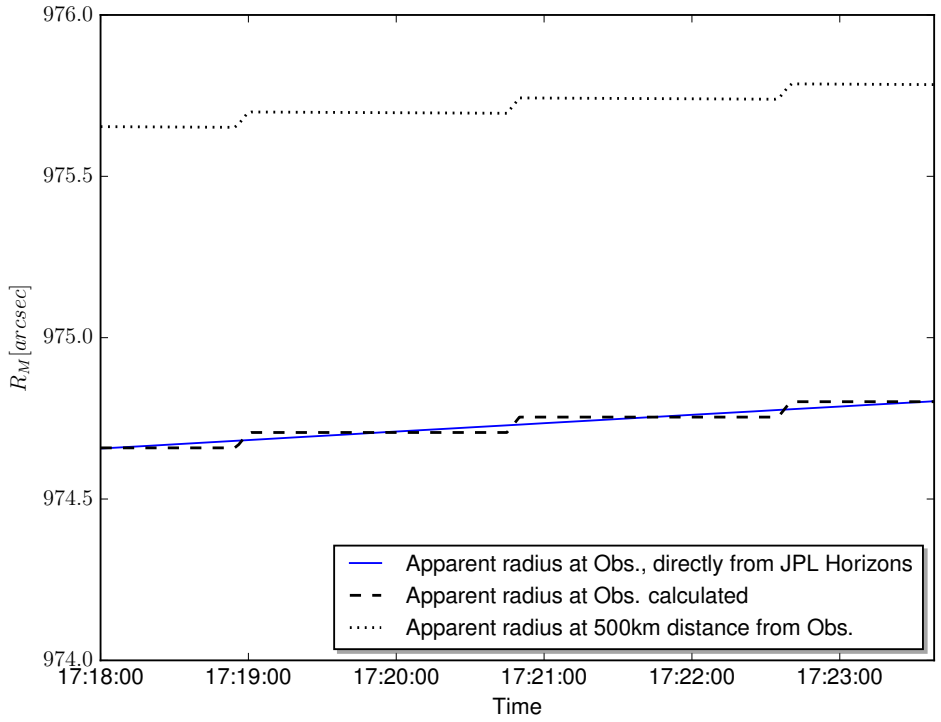

Figure 3.4: Apparent radius of the moon. The blue line shows the values obtained directly from JPL Horizons (category 13), the black lines are based on calculations with the distance of the moon from the observer and the planetary radius as input. The steps in the calculations result from the limited input data precision in the lunar distance.

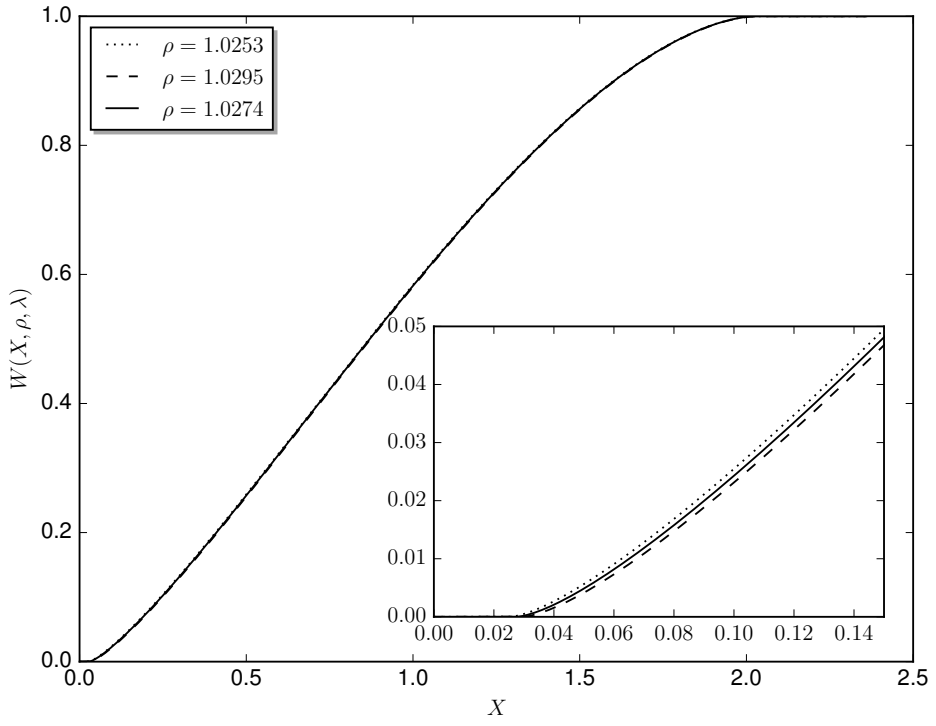

Figure 3.5: The relative solar intensity $w(X, \rho, \lambda)$ compared to the uncovered sun, calculated for $\lambda = 555nm$ with the limb darkening parametrization from Neckel 2005 for different ρ.

3.1.3 Solar Limb Darkening

An important fact one has to consider when integrating over the visible part of the solar disk is the darkening towards the outside of the disk. The cause is that the sun is not a solid sphere with a well defined surface like one might think, but it has a diffuse border like an atmosphere. The part of this solar atmosphere where nearly all the radiation reaching the earth is coming from is called the photosphere. In the solar atmosphere, the same concept of optical thickness like in the earth's atmosphere applies. From this, it follows that photons can not escape the atmosphere without further interaction if they are emmitted to deep inside. In other words, we can only look into the solar atmosphere up to a optical depth of approximately one, for higher depths the atmosphere becomes opaque. The distance of this point of unit optical depth from the center of the sun depends on where we are looking at the disk: Directly at the center, we can see up to deeper layers than looking at the rim. Because the temperature changes between layers, the intensity of emitted radiation at a fixed wavelength also chanes. This effect can be used to determine the vertical temperature distribution in the solar photosphere (Minnaert 1953). Like indicated in Pierce and Slaughter 1977, the temperature gradient shows no difference between the equatorial and polar directions on the sun, so the effect of solar limb darkening is assumed to be spherically symmetric on the solar disk.

In this study, three different parametrizations are used, in order to express the solar limb darkening $\Gamma(r, \lambda)$ through the relative position $r \in [0, 1]$ on the solar disk. The first one by Waldmeier 1955 is the one also used by Koepke et al. 2001 and is based on theoretical considerations, where an expression for the photosphere temperature as a function of optical depth τ was derived, depending on the temperature $T_0(\tau = 0)$. Assuming Planckian radiaton from each volume element in the photosphere and expressing T_0 through the effective temperature of the overall solar radiation T_S, yields the expression in Equation 3.4. h,c and k are the Planck constant, the speed of light and the Boltzmann constant, T_S was set to $5740K$.

$$\Gamma(r, \lambda) = \frac{1 + \beta \cdot \sqrt{1 - r^2}}{1 + \beta} \tag{3.4}$$

$$\beta = \frac{3hc\sqrt[4]{2}}{8k\lambda T_S} \tag{3.5}$$

The other two parametrizations are developed by Pierce, Slaughter, and Weinberger 1977 and Neckel 2005 and are based on measurements from the McMath Solar Telescope at Kitt Peak. In the first case, there were two campaigns (Pierce and Slaughter 1977, Pierce, Slaughter, and Weinberger 1977) where the telescope movement was stopped pointing at the sun, so the sun was passing the small entrance slit. The limb darkening is expressed in a fifth degree polynomial in $\mu = cos(\Psi(r))$ with the coefficients given for discrete wavelengths λ_i in the area between $304nm$ and $1046nm$. Definition of Ψ is shown in Figure 3.6.

$$\Gamma(r, \lambda) = A(\lambda) + B(\lambda)\mu + C(\lambda)\mu^2 + D(\lambda)\mu^3 + E(\lambda)\mu^4 + F(\lambda)\mu^5 \tag{3.6}$$

In order to get the limb darkening at every wavelength λ, a linear interpolation of the limb darkening at the next given values λ_i and λ_{i+1} was implemented.

The data for the parametrization by Neckel 2005 was obtained from measurements in 1986-1990 (Neckel and Labs 1994). These measurements were taken at relatively short intervalls of seven days. The limb darkening function is again expressed in the same form like in Equation 3.6. The coefficients are in turn analytical functions of λ itself

$$A(\lambda) = A_{0,\lambda} + \frac{A_{1,\lambda}}{\lambda} + \frac{A_{5,\lambda}}{\lambda^5}(\text{B,C,D,E,F analog}) \tag{3.7}$$

where the "subcoefficients" $A_{0,\lambda}$,$A_{1,\lambda}$,$A_{5,\lambda}$ are given for the intervalls $300nm - 372.98nm$,$385nm - 422.57nm$ and $422.57nm - 1100nm$ in each case. There is no data for the region around $380nm$ because this part of the solar spectrum is affected by the "Balmer jump". At this wavelength intervall, the continuum of the solar radiation changes due to hydrogen ionization. For wavelengths below the Balmer jump ($364,66nm$ to be exact), photons have enough energy to take the electron completely away from the nucleus, so we have continuous absorption rather than single Fraunhofer lines.

In the last two cases, the limb darkening coefficient was given in dependence of $\mu = cos(\Psi)$ with Ψ defined in Figure 3.6. To express Ψ as a function of r, we derive the following equations:

$$\Psi = \pi - \delta - \gamma \qquad tan(\delta) = \frac{a}{d} \qquad cos(\gamma) = \frac{d}{Rad_S} \tag{3.8}$$

$$d = r \cdot l \qquad l = sin(\alpha) \cdot Rad_S \qquad cos(\alpha) = (\frac{Rad_S}{D_S}) \tag{3.9}$$

$$a = D_S - \sqrt{Rad_S^2 - d^2} \tag{3.10}$$

$$\tag{3.11}$$

Knowing the solar distance from the observer $D_S(t)$ and the radius of the sun $Rad_S = 695.700km$, this allows us to get $\Psi(r)$ by successively plugging the equations into the first one.

In Figure 3.7 the different parametrizations are compared by dividing the results from Waldmeier and Pierce through the values from Neckel. There seems to be an increasing systematic deviation towards the solar limb between Waldmeier and Neckel with the values from Waldmeier generally being higher for shorter wavelengths. Directly at the limb, all the values from Waldmeier exceed the ones from Neckel, in some parts up to 300%. The values from Pierce and Neckel are generally in very good agreement, with deviations of less than 5% in most areas, except at positions extremly close to the solar limb, where the deviation reaches up to 25% without any clear, systematic bias regarding the wavelength.

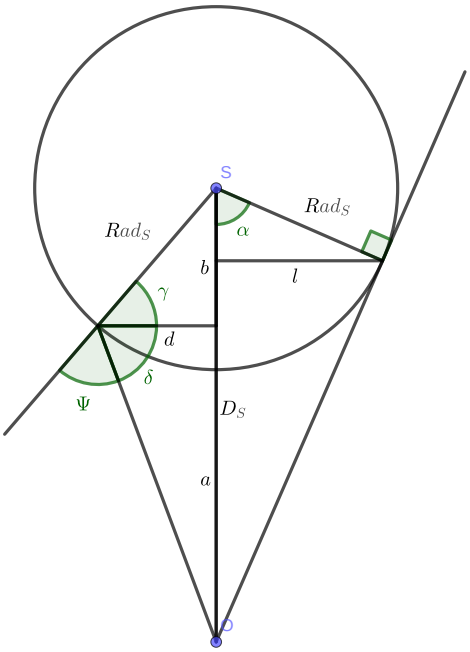

Figure 3.6: Definition of the angle Ψ used in the equations for the limb darkening coefficient.

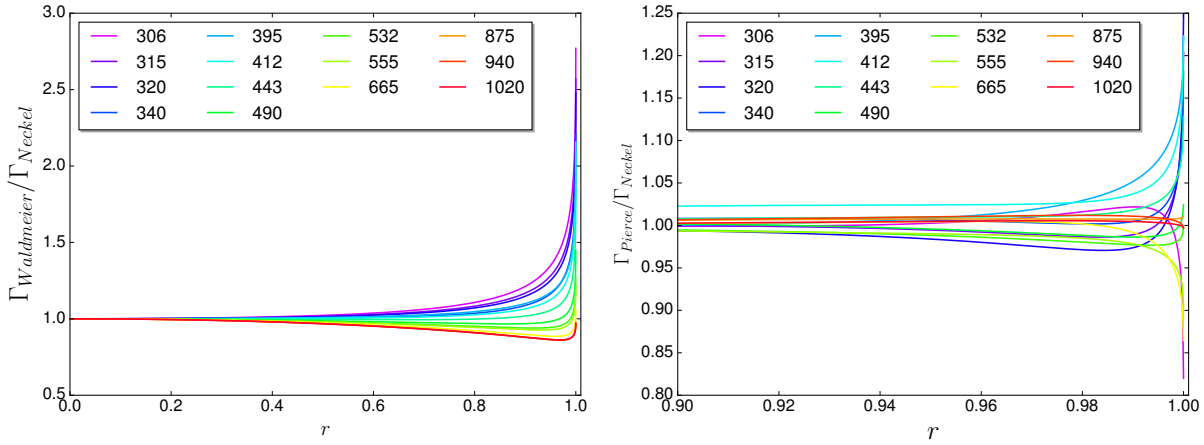

(a) (b)

Figure 3.7: Values of the limb darkening parametrizations from Pierce and Waldmeier, relative to the values from Neckel. Curves are for different wavelengths, given in nm. r denotes the position on the visible solar disk, with $r = 0$ at the center and $r = 1$ at the limb. Note the different scales on the horizontal and vertical axes.

3.2 Atmospheric Part

Having the distribution of solar irradiance at TOA, we need to simulate its effect on the sensor at the earth's surface. This is done with libRadtran, the "library for radiative transfer" (Mayer and Kylling 2005; Emde,

Buras-Schnell, et al. 2016). It is a collection of simulation tools, which allows to calculate nearly every radiation related quantity in the earth's atmosphere one might be interested in. The core is made of the program "uvspec" to read in the input files containig all the information necessary for the simulation of radiative transfer (Unlike the name might suggest, its functionality is not limited to the short wavelength part of the spectrum. The name is mainly due to historical reasons.) One can divide the settings roughly into three parts: settings relating to the state of the atmosphere and environment, settings defining the desired output and information on how to solve the radiative transfer equation numerically. The former depends on the precise conditions of the solar eclipse and is described in more detail for the total solar eclipse 2017 in chapter 4. The latter is generic for all our simulations.

Whenever one dimensional calculations are performed, the radiative transfer solver "disort" was used (Buras et al. 2011). It provides an implementation of the discrete ordinate technique briefly described in section 2.2. All further input settings could be directly adapted from the 3D case, settings referring to other radiative transfer solvers like MYSTIC are generally ignored.

3.2.1 3D LibRadtran settings

To obtain the two dimensional contribution function at TOA, the 3D Monte Carlo solver MYSTIC was applied (Mayer 2009; Emde and Mayer 2007). Because the photons are counted only on one point on the earth, but their origin at the TOA is of interest, it is reasonable to run a backward simulation with *mc_backward*. With *mc_spherical 1D*, the curvature of the atmosphere around the globe is included like described in Emde and Mayer 2007 (Technically, this option enforces a backward calculation automatically). In contrast to a normal cartesian model, photons in spherical geometry are not able to travel infinitely far along one homogenous atmospheric layer. Sooner or later, every photon will hit a boundary layer as a result of the curvature of the atmosphere. Spherical geometry is necessary whenever photons from a very large distance ($1000km$ in our case) could potentially have an impact on the measurements, like it is the case for a solar eclipse. *Output_quantity transmittance* ensures that all calculated quantities are normed to the incoming solar radiation at TOA. The actual contribution from each point is written in '.bac' files if *mc_backward_writeback* is set. It is possible for MYSTIC to produce several of these files, even if only one wavelength is specified. This reflects the fact that, in regions where hydrogen absorption varies strongly, one wavelength may be splitted internally into different bands to produce accurate results, supposed the absorption parametrization REPTRAN (Gasteiger et al. 2014) is set with *mol_abs_param reptran*. The '.bac' files contain the relative portion of each point to the observer signal, normed to the total diffuse transmittance, i.e. the sum of all values in all files should equal the diffuse downward radiation like it can be also obtained with a one dimensional model. The number of bins where the photons are counted is defined with the help of *mc_sample_grid*. The number of photons itself is set with *mc_photons*.

3.2.2 Input and Output processing

Because the position of the sun changes with time, it would be ideal to recreate the contribution function $C(\mathbf{d}, \lambda, t)$ for every timestep. This is however difficult to realize, because the Monte Carlo simulations require high computational effort, depending on the number of photons. To create a flexible solution to produce time series with comparatively low computation time, a small Python wrapper for MYSTIC was written. The program reads in the sun's position from the JPL Horizons data at the desired times and starts a MYSTIC simulation using the specified wavelength. After MYSTIC has finished, the results are written in the aforementioned files. They are weighted with the representative wavelength weights and added together to one final '.bac' file. Only the resulting file is saved with an appropriate header. When producing a time series, the eclipse simulation automatically chooses the '.bac' file matching the simulation time best. This way one could set the temporal resolution of the Monte Carlo simulations at will, depending on the available hard drive space. (one of these resulting files could have a size of up to 0.5Gb. Since empty bins are not stored, this depends on the sample grid resolution and the number of photons traced.)

The photons making up the '.bac' files are all counted at the TOA. Since the TOA is curved in a spherical geometry, the values need to be shifted towards the point in the sampling plane where the photons originally came from. The geometry to do this can be seen in Figure 3.8. We derive:

$$r := z_{TOA} + rad_E \qquad \alpha = \arcsin\left(\frac{\sqrt{x_{0,1}^2 + x_{0,2}^2}}{r}\right) \tag{3.12}$$

$$\mathbf{x_1} = \mathbf{x_0} + t \cdot \hat{\mathbf{k}} = \begin{pmatrix} x_{0,1} + t \cdot sin(\theta_S) \cdot sin(\phi_S) \\ x_{0,2} + t \cdot sin(\theta_S) \cdot cos(\phi_S) \\ r \cdot cos(\alpha) + t \cdot cos(\theta_S) \end{pmatrix} = \begin{pmatrix} x_{1,1} \\ x_{1,2} \\ r \end{pmatrix} \tag{3.13}$$

Solving the third component of Equation 3.13 for t allows the determination of point $\mathbf{x_1}$. Here, the sun is again assumed being sufficiently far away, so that the position (θ_S,ϕ_S) stays constant for movements in the sampling plane.

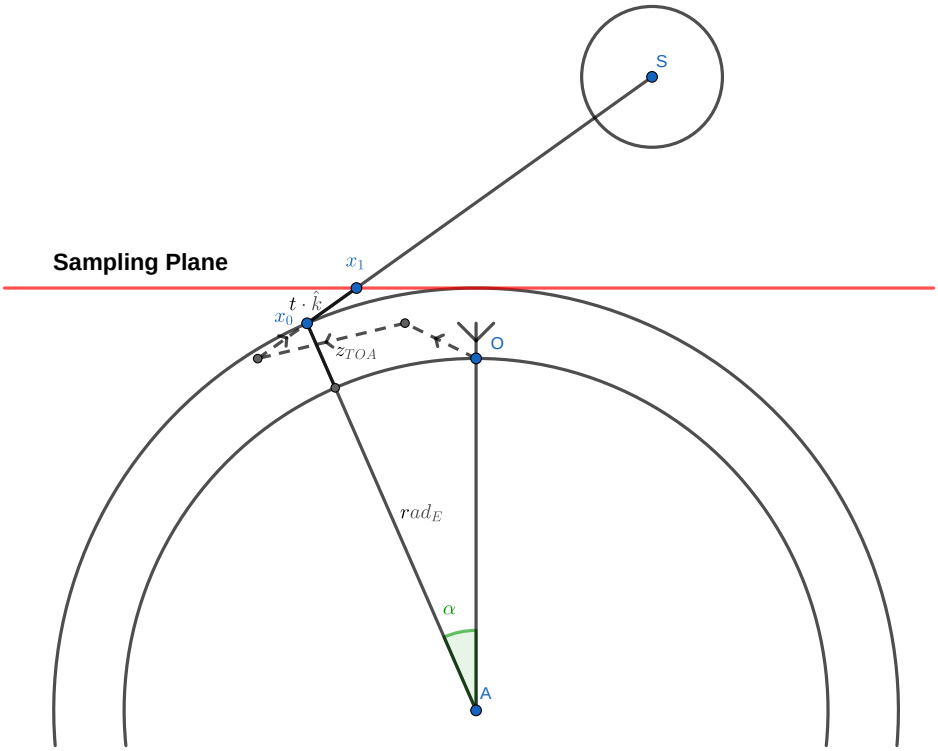

Figure 3.8: Geometry used to associate values in the '.bac' file with values in the sampling plane. The dashed line shows an exemplary photon path.

3.3 Measured Signal

With the solar irradiance weighting function $w(\mathbf{d}, \lambda, t)$ and the contribution function $C(\mathbf{d}, \lambda, t)$ both available, we are now finally able to bring the parts together to obtain the irradiance at the sensor position. Summing up the product of w and C for every point in the sampling plane yields the diffuse fraction of the sunlight reaching the sensor. Because, as already stated above, the light of the sun reaching the sensor directly without any scattering in the atmosphere is not included in the Monte Carlo results, we have to add it as an extra term $w(\mathbf{d_0}, \lambda, t) \cdot T_{dir}$. T_{dir} is the direct atmospheric transmittance, which can be obtained in theory very easy from the Lambert-Beer Law, $\mathbf{d_0}$ is the position where the line from the observer to the sun intersects the sampling plane. At this point, for T_{dir} values computed with 'disort' were used. Multiplying the direct and diffuse fraction of sunlight at the observer position with the extraterrestrial spectrum (ETS) under non-eclipse conditons, finally gives the values we were looking for. Here, it is important to keep in mind that the ETS generally also depends on time. Firstly, the sun's brightness varies in cycles with a period of decades and more, and secondly the earth-sun distance changes by about 3% throughout the year (*NASA Earth Fact Sheet* 2018). The latter is included in a correction factor $\kappa(t)$ in front of the ETS. The formula, the same as implemented in libRadtran, is taken from Iqbal 1983 and is based on a Fourier expansion of the earth-sun distance. The input is the day of year counted from January 1 with 28 days in February. Because the temporal variation is in the order of weeks, it can be kept constant in the simulation of the eclipse with a duration in the order of minutes to hours. The final expression reads:

$$I(\lambda, t) = \kappa \cdot ETS(\lambda) \cdot \left(T_{dir} \cdot w(\mathbf{d_0}, \lambda, t) + \sum_{\mathbf{d} \in SP} C(\mathbf{d}, \lambda, t) \cdot w(\mathbf{d}, \lambda, t) \right) \tag{3.14}$$

$$\begin{aligned} \kappa &= 1.000110 + 0.034221\cos(\gamma) + 0.001280\sin(\gamma) + 0.00079\cos(2\gamma) + 0.000077\sin(2\gamma) \\ \gamma &= 2\pi(day - 1)/365 \end{aligned} \tag{3.15}$$

Chapter 4

The total solar eclipse 2017

The eclipse on which this study will focus mainly is the total solar eclipse that occured on August 21, 2017. It took place in the northern hemisphere, with the umbral shadow starting in the central pacific, passing over the area of the United States, see Figure 4.1a, and finally going further across two-thirds of the atlantic ocean. The penumbral shadow hit the US western coastline at about 16:00UT (9:00PT), before the umbral shadow has its first contact with the earth in the pacific which is at 16:48UT. Measurements were taken in Oregon at 44.362950N and 121.139667W, which corresponds to the red marker in Figure 4.1b. At this place, approximately 37km away from the umbral shadows center line, the eclipse starts at 17:19:46 and lasts for 1:22min. The detailed start and end times at the measurement site can be obtained from Table 4.1. The apparent moon to sun ratio ρ varies for the time of the partial eclipse between 1.0250 and 1.0290. The diameter of the minor axis of the elliptical shadow calculates to 3436km for the penumbral shadow at the time of totality, and 94km for the umbral shadow.

Event	Time[UT]	Elevation[°]	Azimuth[°]
Start partial eclipse	16:06:29	29.4	102.7
Start total eclipse	17:19:46	41.6	118.9
Maximum eclipse	17:20:27	41.7	119.1
End total eclipse	17:21:08	41.8	119.3
End partial eclipse	18:41:05	52.6	143.6

Table 4.1: Times and solar angle for different characteristic events of the eclipse 2017 at the measurement position. Elevation is given relative to the horizon, azimuth is measured clockwise from the north (JPL convention). Created with Espenak 2018.

4.1 Measurements

Measurements of global spectral irradiance at different wavelengths were taken by Germar Bernhard at the above mentioned location, which is situated in Smith Rock State Park, an american state park near Redmond and Terrebonne in Oregon. Details of the measurement conditions and the calibration process will be published separately in another report (Bernhard and Mayer 2018). The following will provide a short summary.

The instrument was placed on a field near the Crooked River and is surrounded by dry gras. In the west and north-east, mountains are obstructing the horizon by up to 12°. The sky this morning was almost clear with only a few clouds near the horizon. It is important to mention that there were several wildfires in the region burning at the measurement time. On the day of the measurement however, the wind direction changed in favor of a decrease of aerosol loading. The instrument used was a GUVis-3511 multi-channel filter radiometer constructed by Biospherical instruments Inc. The sensor was placed approximately one meter over the ground and was equiped with a computer-controlled shadow band to allow the coverage of a defined part of the sky. After the calibration procedure, the channels of the radiometer refer to 306,315,320,340,380,395,412,443,490,532,555,665,875,940,1020, nm respectively.

4.2 Simulations

In this section, the eclipse simulation is applied to the celestial conditions at the measurement site. It is intended to be a proof of concept, verifying that the common features described in Emde and Mayer 2007

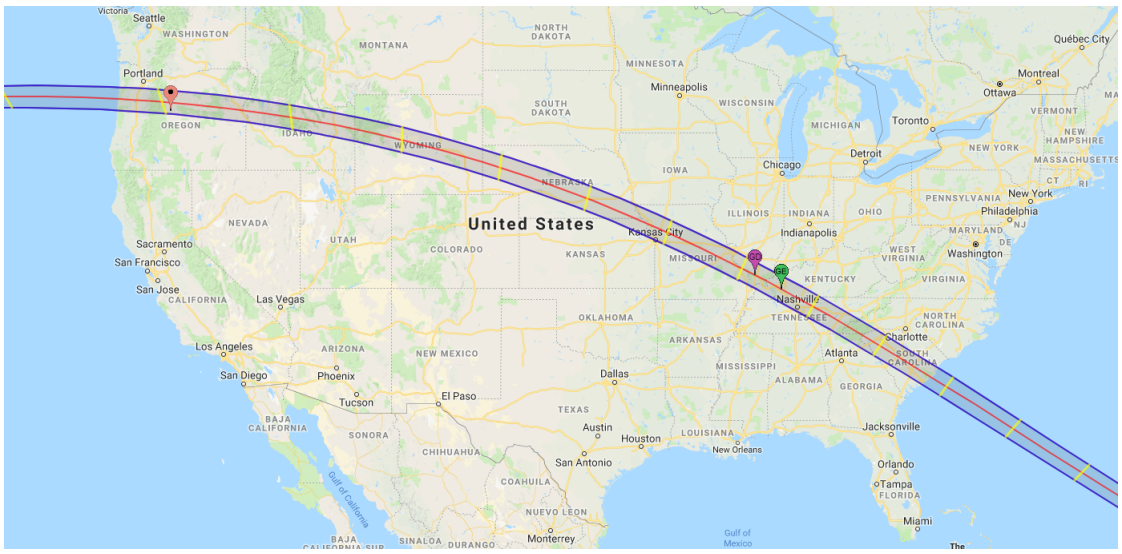

(a)

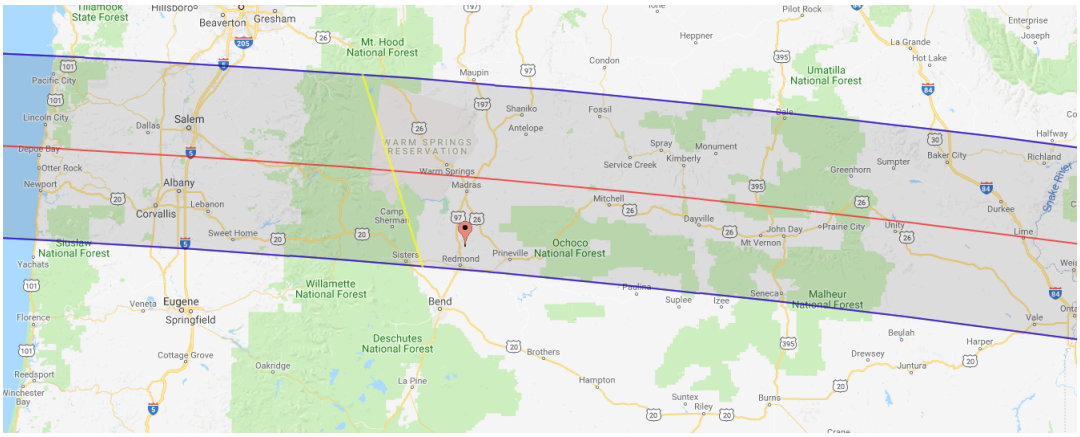

(b)

Figure 4.1: Path of the umbral shadow on August 21, 2017 over the complete US in Figure 4.1a and over Oregon in Figure 4.1b. The red marker shows the measurement position, green and magenta markers show the place of greatest eclipse and longest totality time. Produced with Espenak 2018.

can be reproduced, so the initial atmospheric conditions are kept rather simple. In the following subsections, some of them are examined closer, leading to more realistic results. The celestial data was created with JPL Horizons at the exact position 121°08′22.8″W, 44°21′46.6″N and an altitude of 866.8m. From 14:30UT until 20:00UT the sampling rate was 120s, while from 17:10UT until 17:30UT, the time around the totality, a higher resolution of 5s was choosen. The factor to correct the ETS for the variable sun earth distance is obtained from the formula described in section 3.3 with the day of year set to 233 (August 21). For the solar limb darkening, the parametrization of Pierce and Slaughter 1977 is used. As a first guess for the state of the atmosphere, the profile *afglms*, included in the libRadtran package, was used. It refers to the midlatitude summer atmospheric profile AFGL-TR-86-0110 in G. Anderson et al. 1986 and defines the vertical state of the atmosphere (pressure, temperature, density) as well as the major gas composition (O3, O2, H2O, CO2, N2O). This profile will be refered to as the *midlatitude summer profile* from now on. The thereby specified Ozone profile was scaled to a total ozone column of 298DU. The other profiles are not modified and there are no aerosol options set. Because the "altitude" option in libRadtran is currently not compatible with the spherical backward Monte Carlo model, the values in the profile were interpolated and subsequently shifted down by 866.8m relative to the height scale, to account for the surface height where the measurement were taken. Following the experiences made previously with such simulations in Emde and Mayer 2007, a sampling grid of 2000km x 2000km was used in the horizontal with 1km stepwidth for the contribution function at TOA. 10^7 photons were traced for each wavelength.

Figure 4.2 gives an overview over the change of irradiance with time 10min before and after totality. While the celestial part was fully time resolved, including the sun's position, the atmospheric part is based on one Monte Carlo simulation at 17:20UT. Comparing with Fig. 13 in Emde and Mayer 2007, we can see the same qualitative behaviour. All wavelengths undergo a sudden drop as soon as totality occurs. The

intensity of the 315nm wavelength is remarkably lower than the visible intensities, which is mainly due to ozone absorption. This might also be the reason for the stronger coupling of irradiance to the distance from the shadow center for shorter wavelengths. For all wavelengths, there is a slight asymmetry in the irradiance gradient at the beginning and at the end of the eclipse. This can be attributet, as also explained in Emde and Mayer 2007, to the contribution function at TOA. Most of the diffuse photons originate from a line at TOA between the point directly above the observer and the intersection point of the observer-sun line with the TOA. Photons from this line can reach the observer being scattered only once. Because the sun is located in the South-East and the lunar shadow travels from East to West like it can be seen in Figure 4.3, the single scattering photons are covered before the direct beam vanishes at the beginning of totality. As soon as the latter happens, irradiance makes a sudden drop. In the second half of totality, the single scattered photons are released step by step, resulting in a measureable increase of irradiance since the direct solar beam is still suppressed. As soon as this is not the case anymore, it outweighs the diffuse radiation. Looking at the longer infrared wavelengths, one finds that they decrease by nearly four orders of magnitude, leading to totality intensities almost as low as in the UV-part of the spectrum. The reason is the proportionality of the Rayleigh scattering cross section to $\frac{1}{\lambda^4}$, making the scattering into the umbral shadow much less efficient than it is for shorter wavelengths.

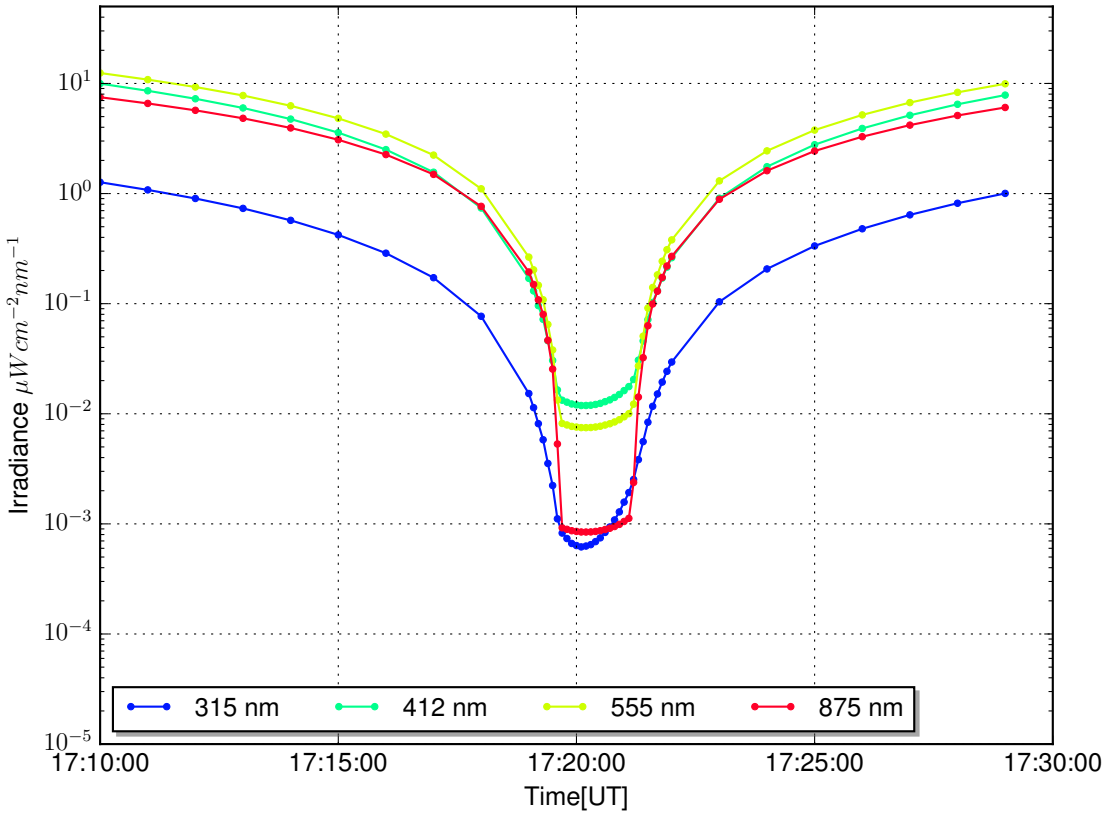

Figure 4.2: Time series of irradiance for different wavelengths $10min$ before and after totality.

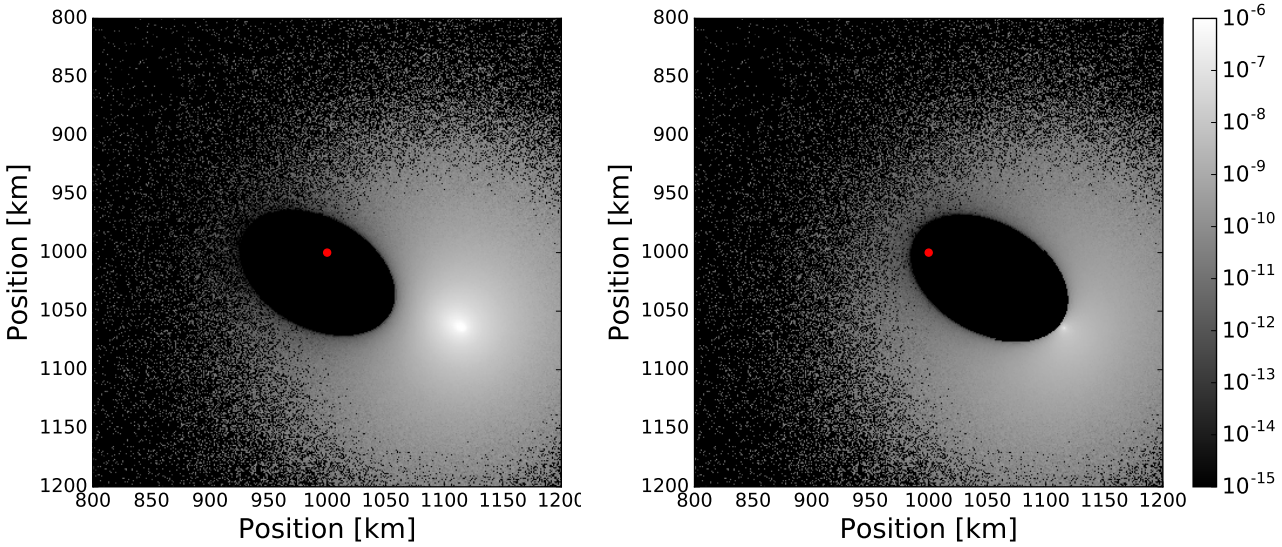

(a) 17:18:30

(b) 17:19:30

(c) 17:20:30 Totality

(d) 17:21:30

Figure 4.3: The umbral shadow moving from West to East in the sampling plane. Shown is the 400kmx400km part around the observer, which is indicated by the red dot. The colorbar gives the fraction of intensity coming from each pixel at 315nm, relative to the extraterrestrial 315nm intensity under normal conditions.

4.2.1 Surface Albedo

So far, all the results were produced with a spatially and spectrally constant Lambertian surface albedo of 0.05. This does not seem to be a very reasonable assumption since, especially in the infrared, the albedo over vegetation can reach values up to 0.5. Figure 4.5a shows how the 315nm and 875nm channel change when the surface albedo is set to 0.5, compared to the previous results with 0.05. For places outside the umbral shadow, the 875nm band is virtually not affected due to the large fraction of direct radiation contributing to the signal. In the ultraviolett, where more light is scattered, the brighter surface around the observer can increase the irradiance between 10% and 20%. Throughout the totality, there is a clear difference for both channels, where the irradiance increases by a factor of 1.6 in the UV and by 2.0 for the infrared wavelength. At the time of the measurements, the environment around the sensor was mainly covered by dried vegetation. Sattellite pictures show mostly beige to light brown colors in the area. The first step to get a more realistic albedo setup is to use a wavelength dependent, spatially constant surface albedo representing the surrounding area. For this task, there are two large public online libraries available which list reflectances of various materials, hosted by the JPL (*ECOSTRESS spectral library* 2018), respectively by the US Geological Survey (*U.S. Geological Survey Spectral library* 2018). From the latter, the dataset AV87-2 was used, which refers to dry, long grass, shown in Figure 4.4a.

The behaviour of irradiance over the full spectrum can be seen in Figure 4.5b. The aforementioned characteristics are also visible in this graph: There is a difference of about 20% for the UV wavelengths with constant surface albedo outside totality, which decreases relatively smooth towards the infrared channels. If the spectral albedo distribution in Figure 4.4a is applied, there is almost no difference in the irradiance over the complete spectrum, compared to a black surface. The strong increase in the grass' albedo is cancelled mostly by the decreased sensitivity of the irradiance towards changes in the surface reflectance. This is obviously not the case any more as soon as totality starts. Setting the albedo from 0.05 to 0.5, the corresponding curve in Figure 4.5b reveals a strong wavelength dependence, the change of a factor 2.0 is only true for 875nm. There are two conspicous dips around 720nm and 940nm, indicating a coupling between the albedo sensitivity and water vapor absorption. Absorption might also be the reason for the decreased sensitivity in the ultraviolett. In general, an absorbing medium suppresses longer photons paths, which in turn are more likely to interact with the surface. Qualitatively, this behaviour is also valid for the grass albedo, however with a smaller effect due to the lower albedo values and and increasing values resulting from the increase towards longer wavelengths.

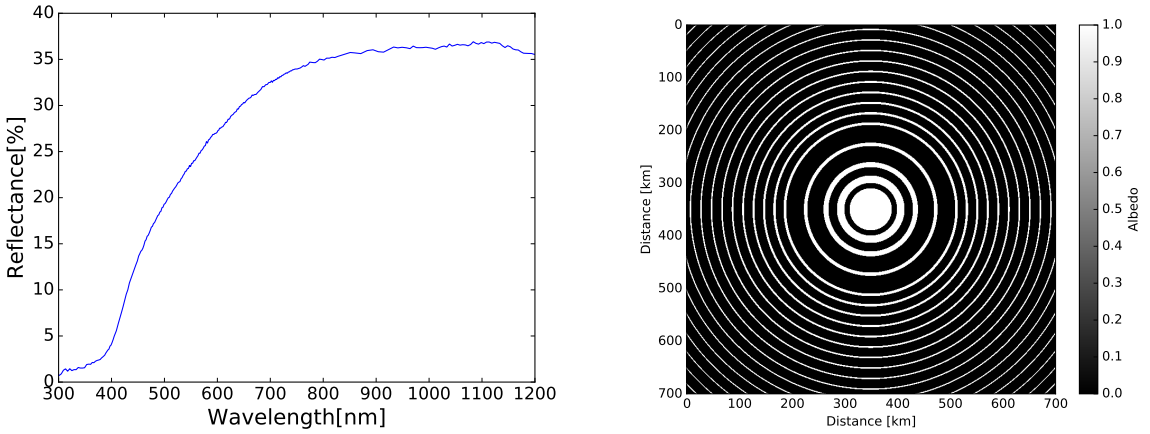

(a) Reflectance of dry, brown vegetation. Dataset AV87-2, *U.S. Geological Survey Spectral library* 2018.

(b) Rings of albedo 1.0 with a constant area of $5000km^2$, like they are used in Figure 4.7b. They were combined in one map only for visualization.

Figure 4.4: Basis for the spectral and spatial variation of the surface albedo.

A change in irradiance of up to 200% only due to the surface albedo is quite remarkable. For a future implementation of detailed maps of the surrounding, it is necessary to know the influence of different areas in the simulation domain, in order to choose an appropriate resolution of the maps. Therefore, in this second part of the albedo study, several simulations were performed with circles and rings of albedo 1.0 on an otherwise black surface of albedo 0.0, centered around the observer. An example with several rings can be seen in Figure 4.4b. The maps can be integrated in MYSTIC with *mc_albedo_file*. All following simulations correspond to 17:19:55UT, wavelength was kept constant to $555nm$.

In Figure 4.6, fully filled white circles were used. The derivative of the relative irradiance with respect

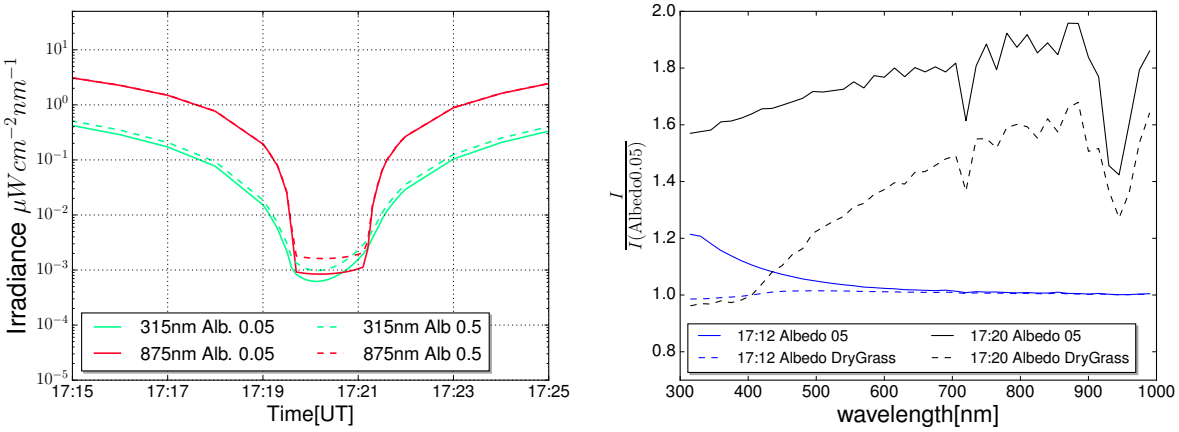

(a) Influence of the surface albedo on the irradiance for wavelengths of 315nm and 875nm.

(b) Relative spectral irradiance at 17:20UT and 17:12UT for different spectral distributions of the surface albedo. Values are normed to the values obtained with an albedo of 0.05 ("005").

Figure 4.5: Temporal and spectral variation of irradiance.

to the circles radius r, expresses the influence of areas located in a distance r. From this, it can be seen that areas in a distance between $20km$ and $400km$ are the reason for most of the observed changes. The albedo of areas more than $600km$ away from the observer has almost no effect on the measurements. In our case, this means the Pacific in the western part of the simulation domain can be neglected for example. Generally, areas in greater distance contribute less photons to the result than nearer areas with the same size, which is however compensated by the growth of the circle area proportional to r^2. This leads to a maximal influence for the region around the observer in $100km$ distance.

The influence of the surface albedo *per area* is studied in Figure 4.7a and Figure 4.7b, where rings with constant area rather than circles are used. The graphs reveal that the maximum in the derivative in Figure 4.6 is indeed attributable to the increasing circle surface, whereas the influence of a surface element with unit area decreases the further away it is from the observer. Although there were 10^8 photons traced for each ring, there is clearly some noise in the curves as soon as the changes are in the order of 1% and less, making it difficult to examine the nearest area around the sensor. The smallest ring in Figure 4.7a still has an outer radius of $18km$.

An ideal map should therefore cover the surrounding up to a distance of at least $400km$, possibly at the cost of a lower resolution. If there is the additional possibility to make high-resolution measurements of the surface albedo for a certain amount of area, the efforts should focus on the direct surrounding of the observer at first.

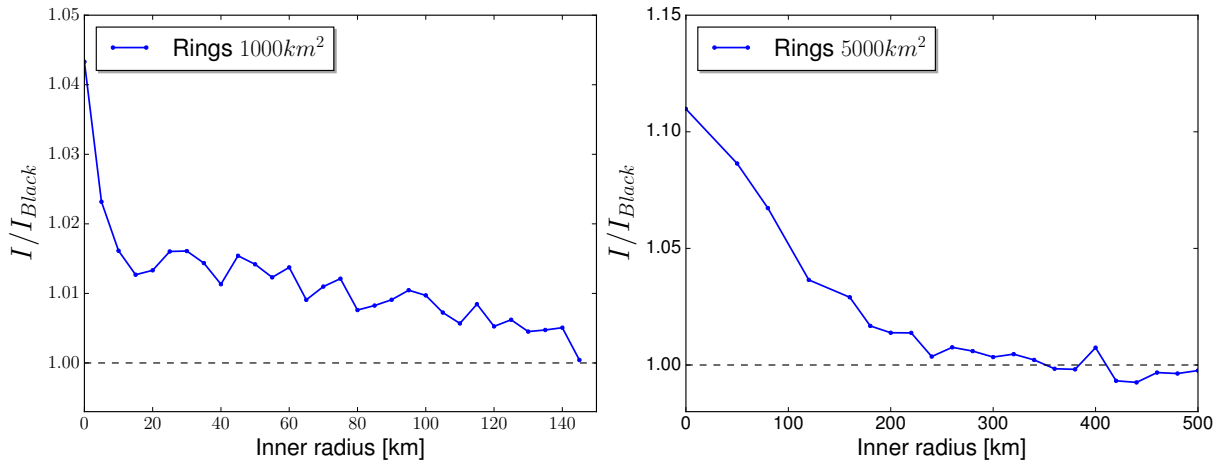

(a) Ring Area $1000km^2$

(b) Ring Area $5000km^2$

Figure 4.7: Irradiance at 17:19:55UT and $555nm$ for white rings with different inner radii, relative to the irradiance from a black surface. The area of the rings was kept constant.

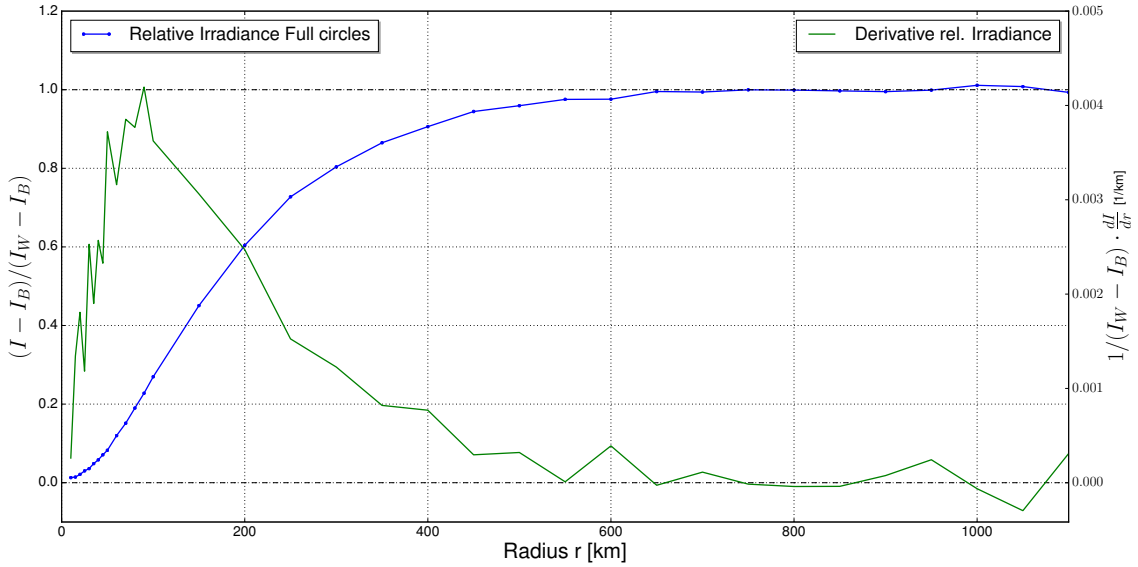

Figure 4.6: Blue graph: Change in irradiance at 17:19:55UT and $555nm$ for white, filled circles with different radii. Shown is the difference to the values from a black surface (subscript B), normed to the difference if the surface is completely white (subscript W). In the latter case, irradiance is increased by a factor 2.96 compared to the black surface. The green graph shows the derivative with respect to the circle radius.

4.2.2 Ozone profile

A trace gas which has a remarkable influence especially on the UV part of the spectrum is Ozone. In the following, a sensitivity analysis like already done for the albedo is performed. In general, the total column of ozone (TOC) in the atmosphere, regardless of the height profile, is measured in Dobson Units [DU]. One Dobson Unit is the thickness, in $10\mu m$ steps, of a layer of pure Ozone at $273.15K$ and $10^5 Pa$. The total column at the measurement site can be gained from comparisons between the $305nm$ and $340nm$ channel of the instrument at times outside the eclipse and a look-up table created with a radiative transfer model. Details of this derivaton are described in Bernhard and Mayer 2018. The measured values for the TOC are $293DU$ directly before the eclipse and $294DU$ after the end. These values can be compared with measurements of TOC from the Ozone Monitoring Instrument (OMI), mounted at the Aura satellite. A quick access to the data can be obtained for example via *NASA World View* 2018. For the measurement position, there is no data available at the day of the eclipse. The day before, a value of $297DU$ was measured there. However, looking at the simulation area for different days before and after the eclipse, a TOC between $280DU$ and $320DU$ is within the range of possible values. To test the influence not only of the TOC, but also of the vertical distribution of ozone, a vertical profile produced with MOZART, the Model for Ozone and Related Chemical Tracers (Emmons et al. 2010), is used. The ouput was requested for August 21, 2017 and evaluated at the horizontal grid cell 44.5°N, 120°W. MOZART outputs the ozone concentration as volume mixing ratio (VMR) for every grid cell, where the vertical position is specified in hybrid sigma-pressure coordinates. They represent a compromise between sigma pressure and pure pressure coordinates, following the terrain smoothly at the surface and transforming into levels of constant physical pressure the higher it gets in the atmosphere. The physical pressure at any level k in the model was calculated by

$$P(x, y, k) = A(k) \cdot P_0 + B(k) \cdot P_S(x, y) \tag{4.1}$$

The height information is completely contained in the coefficients A and B, for which the MOZART variables "hyam" and "hyab" where used, referring to the center of mass of the grid cells. P_0 is a constant reference pressure, $P_S(x, y)$ the surface pressure, accessible over the fields "P0" and "PS". After the change from hybrid to pure pressure, the ozone concentrations were interpolated linearly to the pressure values in the midlatitude summer profile and converted into the number of particles per cubic centimeter, with the use of the temperature profile defined in the midlatitude summer profile. Because the ozon concentrations from MOZART are only available between $1.8hPa$ and $877hPa$, the values outside this range were not adapted. For the values over $877hPa$, this is compensated for the most part anyway, when the modified midlatitude summer profile is again interpolated and shifted $866m$ to account for the height of the sensor. An overview over the original and scaled ozone profiles is given in Figure 4.8. The TOC is calculated from the profiles by integrating the concentrations over the height and converted to Dobson Units with the use of the ideal

gas law ($PV = NkT$). Scaling was done subsequently with a global factor of 298/304 respectively 298/340. With $304DU$, the prediction of the unscaled MOZART profile is already close to the measured values from OMI and at the ground. The midlatitude summer profile has an additional amount of ozone in the lower stratosphere between $10km$ and $20km$. Therefore, scaling it results in a shift of approximately $15DU$ from the higher stratosphere towards the tropopause, compared to scaled version of the MOZART profile. This can be seen in detail in Table 4.2.

Results can be seen in Figure 4.9. There was again no aerosol specified in the simulations, but the albedo file for dried grass introduced in subsection 4.2.1 was set to produce more realistic results. To account for the small differences when changing ozone for some wavelengths, the number of photons traced in the simulations was increased to 10^8 per wavelength. Outside the totality at 17:12UT (Figure 4.9a), a change in the total ozone column leads to increased irradiance like one would expect it for a reduction of an absorbing gas. The sensitivity depends strongly on the ozone cross section, causing changes in irradiance of $\pm 20\%$ at $304nm$ and $\pm 0.5\%$ around $600nm$. Around $400nm$ and above $750nm$, the influence of ozone vanishes.

A change in the ozone distribution instead of the column has almost no influence outside the UV region, where the direct irradiance, which for both profiles has to pass the same TOC, dominates. In the UV part of the spectrum, the irradiances increase with more ozone in the upper atmosphere using the profile from MOZART. This indicates that most of the photons still travel below the stratopause. Results inside the totality agree with the results outside in the typical features. Due to the missing direct radiation, the sensitivity to ozone is generally increased, with changes of up to $\pm 30\%$ at $304nm$ and $\pm 2\%$ at $600nm$. Since the actual intensities are much smaller, there are nevertheless more statistical fluctuations in the results. Without the direct solar radiation, it is now possible to see the influence of the difference between MOZART and the midlatitude summer profile also around $600nm$. The curve is close to the one with $280DU$.

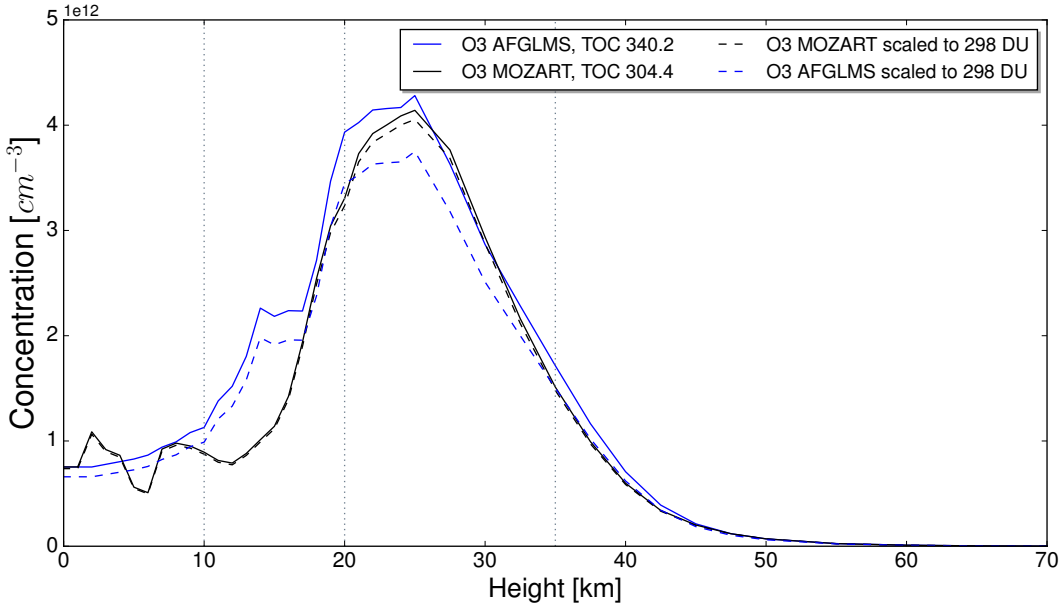

Figure 4.8: Ozone concentrations for different heights above sea level like specified in the midlatitude summer profile and MOZART. The vertical dashed lines indicate the layers refered to in Table 4.2.

Height	Mitlatitude Summer	MOZART
$0km$ - $10km$	$28.85DU$	$30.90DU$
$10km$ - $20km$	$73.79DU$	$57.90DU$
$20km$ - $35km$	$165.33DU$	$179.74DU$
$35km$ - $120km$	$30.03DU$	$29.46DU$
$Total$	$298DU$	$298DU$

Table 4.2: Total ozone column for different layers in the scaled midlatitude summer profile and MOZART profiles. Heights measured above sea level. There is a shift of about $15DU$ from the lower to the upper stratosphere in MOZART.

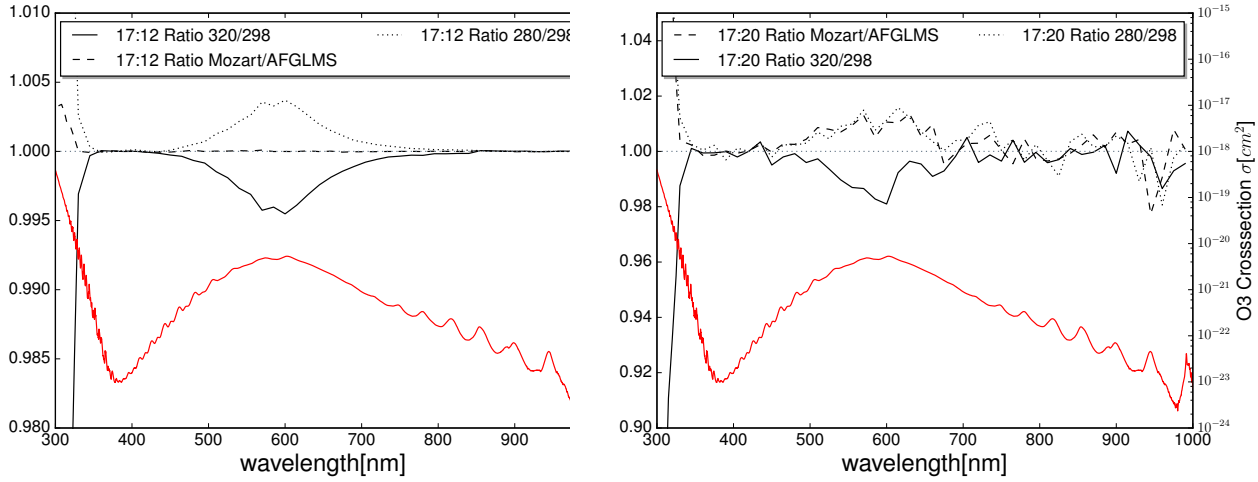

(a) Outside Totality (17:12UT)

(b) Totality (17:20UT)

Figure 4.9: Simulated irradiances for different wavelengths, normalized to the irradiance at the corresponding wavelength with the midlatitude summer profile scaled to 298DU TOC. The blue line is located at 1.0. The red curve shows the total ozone cross section, referenced to the right axis. Note the different scales inside and outside totality.

4.2.3 Topography

In subsection 4.2.1, a first adaption of the simulation to the surrounding area was made by the implementation of a more realistic surface albedo profile. In this section, a further adaption to the environment around the measurement device will be made by analysis of the surface elevation. As it is clearly visible in the photo in Figure 4.11a, the environment is not plain, but contains some mountains nearby, especially in the west, north and east. A topographical map of the area is given in Figure 4.11b, where two exemplary hilltops are marked with their height and distance relative to the observer. For these two positions, the visible angle of the horizon covered by mountains can be directly calculated using $\alpha = atan((h_{Hill} - h_{Obs})/Dist)$ to 10.6° for the western hilltop and 11.2° for the mountain north-east. A more detailed profile is derived from a 360° panorama, showing the view as seen from the measurement location in Bernhard and Mayer 2018. The values, averaged over azimuth intervals of 22.5° and sampled in the order east-south-west-north-east, are listed in Table 4.3

E				S				W				N			
0	22.5	45	67.5	90	112.5	135	157.5	180	202.5	225	247.5	270	292.5	315	337.5
7°	7°	5°	5°	5°	3°	2°	2°	7°	7°	3°	9°	7°	7°	9°	7°

Table 4.3: Azimuth angle (second row) and corresponding height of the mountains over the horizon (third row) in °. Values taken from Bernhard and Mayer 2018

A physical correct implementation of the mountains would require a high resolution 3D surface map, together with the corresponding albeo map including the hilltops as well as the tilted sides of the mountains. While this could be done theoretically with MYSTIC, at least in a non-spherical geometry, data with sufficiently high resolution for larger areas is rare. Nevertheless, the effect of the mountains on the measured irradiance could be estimated to the first order with the assumption of completely black mountains, effectively blocking all the radiance reaching the sensor from their particular direction. If radiance would be coming isotropically from all directions, the relative amount of irradiance blocked by mountains in direction ϕ of height $\theta_m(\phi)$ could be easily calculated to be

$$\frac{\int_0^{2\pi}\int_{\pi/2-\theta_m(\phi)}^{\pi/2} L\cos(\theta)d\Omega}{\int_0^{2\pi}\int_0^{\pi/2} L\cos(\theta)d\Omega} = \frac{1}{2\pi}\int_0^{2\pi}\sin^2(\theta_m(\phi))d\phi = \sin^2(\theta_m) \tag{4.2}$$

The last equality holds for mountains of equal height fully surrounding the observer. In the aforementioned case with 10°, a reduction of 3% in diffuse irradiance could be expected.

This is certainly not true anymore during totality, where an anisotropic radiance distribution is highly likely. To estimate the amount of blocked irradiance, an efficient way is to modify the code of the backward

Monte-Carlo model, setting the weight of every photon starting into directions below $\pi/2 - \theta_m(\phi)$ to zero. Results can be seen in Figure 4.10. Simulations were done with the scaled MOZART ozone profile introduced in subsection 4.2.2 and the dry grass albedo from subsection 4.2.1. There were three spectral series produced, one without mountains ($\theta_m = 0°$), one with $\theta_m = 10°$ and one with the mountain profile around the sensor at the measurement site 2017 shown in Table 4.3. The last series will be denoted as "2017". The overall trend shares many characteristics with the curves in Figure 4.5b, where the surface albedo was changed. Eight minutes before the totality, changes of up to 2% can be observed for the shorter wavelengths. This is already an indication for a disproportionally high amount of diffuse photons coming from the horizon, since direct irradiance, which is not affected by the mountains, still makes up the biggest part of the signal at this time. The increasing direct irradiance is also the reason for the vanishing differences at longer wavelengthts. Observations during totality confirm the importance of horizontal photons, with reductions in irradiance of up to 60%. Like already noticed before, now the longer wavelengths are more sensitive towards changes in the surrounding. Again, there are two clearly visible spikes in regions of high absorption, where longer photon paths are suppressed: here, contribution from photons with shorter ways through the atmosphere is enhanced, which therefore are coming from higher angle positions over the hilltops. Between the 10° mountains and the 2017 profile, there are no major differences despite the lower decrease due to the lower average mountain height in 2017. One might summarize: The higher absorption and scattering for a certain wavelength, meaning the higher the extinction coefficient, the shorter the mean photon paths and therefore the lower the relative influence of albedo and surface elevation on the irradiance signal at totality.

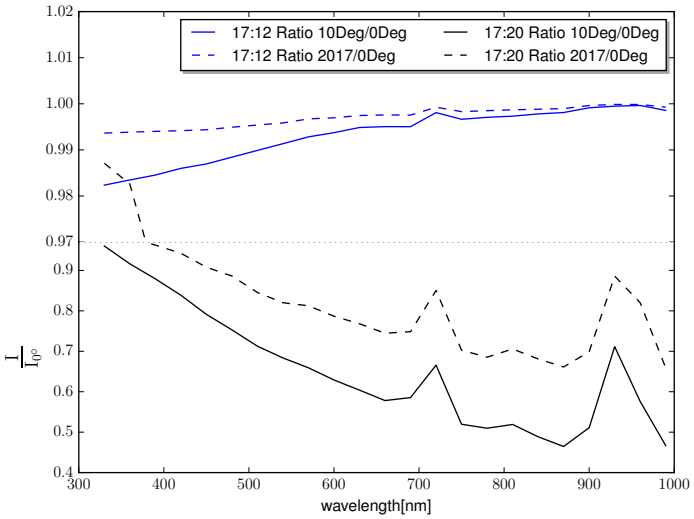

Figure 4.10: Simulated irradiances for different wavelengths and mountain heights, normalized to the irradiance at the corresponding wavelength without mountains. Note the scale change on the y-axis indicated by the dashed, grey line. Blue lines are values outside totality, black lines during totality. "2017" denotes the mountain profile for the measurements 2017 from Table 4.3.

(a)

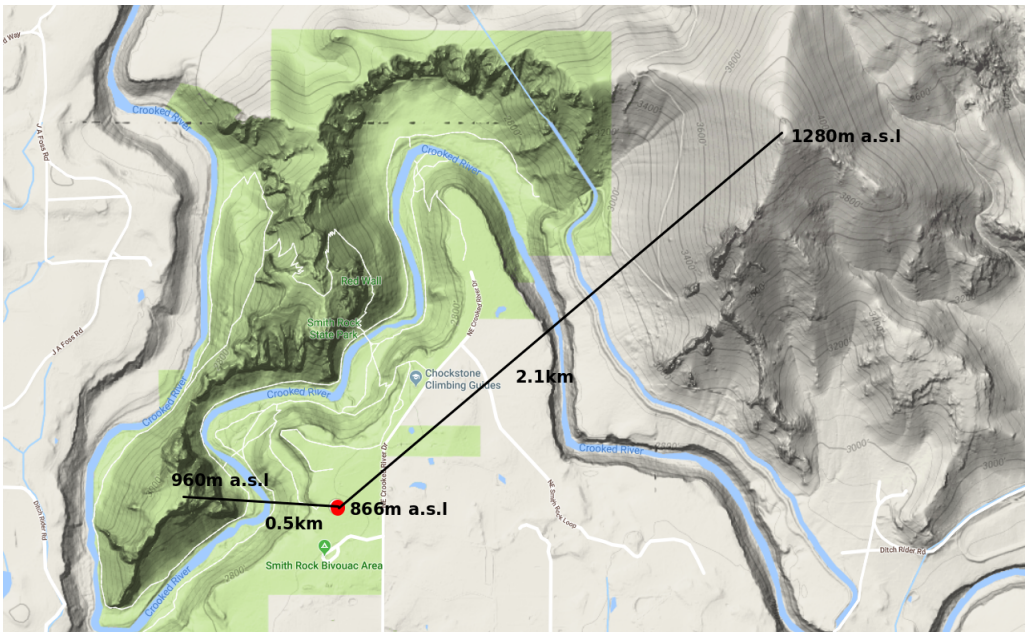

(b)

Figure 4.11: Figure 4.11a shows a photo of the measurement site, taken from the mountain in the upper right in Figure 4.11b. The point of the instrument is indicated by the red arrow. Figure 4.11b shows an elevation map, where the instrument is located at the red dot. Two exemplary mountains are marked with distance and height. It can be seen that roughly three-fourths of the observing point are surrounded by mountains. Created with *Google Maps* 2018.

4.3 Comparison with measurements

The measurement curves shown in the following are based on a combination of two different data sets with and without shadowbanding. There are some short gaps in the time series, where the irradiance measurements were interrupted. Shortly before and after totality, the moments when the remaining direct solar radiation is covered by the shadowband and irradiance drops by more than one order of magnitude for a few seconds, were also removed to avoid sharp spikes in the ratio of measurement and simulation. Global irradiance was measured with a sampling rate of $1Hz$, for periods of shadowbanding, the rate was increased to $15Hz$. Whenever there are multiple measurements within one second intervals, they are averaged to obtain one value per second.

The measured irradiance values after the sensor calibration process are given in units of radiated power per area, referencing to spectral intervals of $1nm$. To reproduce these values, the transmission of the atmosphere was simulated for exactly one wavelength per channel. Afterwards, the result was weighted with the extraterrestrial solar irradiance spectrum convoluted with a $1nm$ FWHM triangular function. This implies the assumption that atmospheric transmission is sufficiently constant within the response interval of the channels. Up to $675.5nm$ the spectrum 2004JD004937-ETS_GUEYMARD described in Bernhard, Booth, et al. 2004 and available at http://uv.biospherical.com/Version2/Paper/2004JD004937-ETS_GUEYMARD.txt was used. Above 675.5 nm, the extraterrestrial spectrum published by Gueymard 2004 was used. In the Monte Carlo simulations, $2 \cdot 10^7$ photons were traced per wavelength. The atmosphere was initialized with the midlatitude summer profile, together with the ozone distribution from MOZART, scaled to $298DU$. The environment was modeled with the mountain profile introduced in subsection 4.2.3 and the dry grass albedo from subsection 4.2.1. Solar limb darkening was calculated with the parametrization from Pierce and Slaughter 1977. The aerosol settings were the ones proposed by Bernhard and Mayer 2018, based on measurements at 19:00UT. They are listed together with the corresponding libRadtran parameters in Table 4.4. The column of precitable water was set to $11kgm^{-2}$, scaling the mitlatitude summer profile. The value was choosen to achieve best agreement between the measurements from 19:00UT to 20:00UT and the $940nm$ channel, which is strongly influenced by water vapor. This is comparable to the value $13.85kgm^{-2}$ from the ERA-Interim global reanalysis, produced by the European Centre for MediumRange Weather Forecasts (Dee et al. 2011) The reanalysis was evaluated at 08.21.2017, 18:00UT at the grid point 44.25N, 121.5W. The 3D simulation is done with 100 equidistant time steps between 17:18UT and 17:23UT, with the contribution function at 17:20UT used.

Parameter	Value	Description
aerosol_default	-	Setting libRadtran default profile for spring-summer conditions.
aerosol_visibility	50	Aerosol horizontal visibility
aerosol_haze	1	Rural type aerosol in the lower 2 km
aerosol_season	1	Spring summer profile
aerosol_vulcan	1	Background aerosols above 2 km
aerosol_modify ssa set	0.95	set the single scattering albedo
aerosol_modify gg set	0.7	set the asymmetry factor of the scattering phase function
aerosol_modify angstrom	$\alpha = 2.1$; $\beta = 0.0394$	Set the integrated optical thickness to $\tau = \beta\lambda^{-\alpha}$

Table 4.4: Aerosol settings according to Bernhard and Mayer 2018

4.3.1 Clearsky

The complete measurements cover the range from 14:30UT until 19:30UT and are shown in Figure 4.12 together with simulated time series of irradiance for clearsky conditions, i.e. if no eclipse would occur. The simulations were done with the RTE solver disort in a 1D setup, with only the solar zenith angle depending on time. The effect of the mountains is not included in these simulations. Looking at the measurements, the drop of the eclipse is conspicous, with the first signs already 1:20 hours before totality in accordance with Table 4.1. In the morning during sunrise, before the eclipse starts, the curves are not as steady as around noon, which is very likely attributable to clouds and aerosol. After the end of the eclipse around 18:45UT, all of the simulated wavelengths agree within 5% with the measurements. The only exception is the $315nm$ channel with a difference of 8%, which might be due to uncertainties in the ozone profile or TOC.

To correct the simulations from possible systematic parametrization errors that have nothing to do with the eclipse, the average ratio of the clearsky simulations and the measurement at all times after 19:00UT

is calculated. This correction factor is from now on applied to all simulated values. The outcome for clearsky conditions can be seen in Figure 4.13. For times after 19:00UT, the curves agree per definition. The plausibility of this correction is confirmed if one considers the times before the start of the partial eclipse. All of the wavelengths agree at 16:00UT within 3% with the measurements. Before 16:00UT, the cloud/aerosol influence is obvious.

4.3.2 Totality

The results of the 3D calculations from 17:18UT until 17:23UT can be seen in Figure B.1, Figure B.2 and Figure B.3, divided in three wavelength domains. In each case, the corrected simulations and the measured values are shown in the upper part of the figure. In the lower half, the measurement was divided through the simulation. Both series were interpolated linearly before the division. There are some characteristics all three domains have in common. For the most part of the totality, from 17:20:00UT until 17:21:15UT, the shadowband swiped over the sensor and reduced the measured irradiance. This area is indicated by the grey gap in the time series. The corresponding curves including the times of shadowbanding can be seen in B. In all three domains, there are two spikes in the ratios directly before and after the totality, where the temporal gradient of irradiance is very strong. Here, the measurements exceed the simulation up to a facor of 1.6, giving information about temporal uncertainties which are intensified in this regions. Because the peaks indicate reduced simulations both before and after the totality, the deviation is likely not a temporal shift in one direction, but a too long persisting totality of about $1-2$ seconds (a pure shift would result in higher values on one side, and lower values on the other). The reasons could be manifold, e.g. small errors in the lunar radius could change the shadow's size easily and therefore affect the totality time. According to Young 2018, a detailed implementation of the lunar limb profile could change the shadows position on earth between $1km$ and $3km$. With a speed of the shadow of about $1000m/s$ for the eclipse 2017, this results in uncertainties of $1s$ - $3s$.

Looking at the wavelength domains separately, the best results are achieved between $400nm$ and $600nm$. Agreement outside the totality is within 3%, during totality the values agree within 10%. There are several reasons why these wavelengths are easier to simulate and measure. On the one hand, their clearsky intensities exceed the other domains by a factor of at least 1.5 (compare Figure 4.13), on the other hand, there are only few absorbing trace gases. Ozone absorption plays a role mostly below $400nm$, water vapor absorption gets relevant especially from $700nm$ on. An overview on the absorption features is given in Figure 2.1. However, there seems to be a systematic deviation towards longer wavelengths being simulated to high during totality. From the sensitivity analysis, one could attribute this maybe to the TOC, affecting the $500nm$ - $700nm$ range only during totality, but this would in turn lead to massive changes in the ultraviolett, leading very likely to worse results there. Moreover, the amount of ozone required to affect the $555nm$ by 10% would be unrealisticly high, comparing with Figure 4.9b.

For $600nm$ - $1020nm$, the results are comparable, with somewhat more fluctuations due to the lower solar intensities. The $1020nm$ cuve shows nearly perfect agreement regarding the intensities, but the temporal uncertainty is one of the highest for all channels. $665nm$ shows better temporal agreement, but continues the trend of higher simulation results at totality also described for the $400nm$ - $600nm$ domain. As already mentioned, the $940nm$ channel depends highly on the water vapor concentration in the atmosphere, a quantity with typically large fluctuations in time and space. For example, the ERA-Interim reanalysis shows values in the order of $10kgm^{-2}$ to $20kgm^{-2}$ for the water vapor concentration in the $2000km$x$2000km$ simulation domain. Nevertheless, the agreement outside the totality is as good as for the other wavelengths in this domain. Of course, one has to remember that the total water vapor column was scaled to fit this channel. Inside the totality, there is too much noise in the $940nm$ measurement signal to make a precise statement, although the mean value seems to fit the simulation pretty well (compare also Figure 4.17a).

Between $300nm$ and $400nm$, the quality of the results does not achieve the one of the other wavelength domains. Since the intensities are comparabely low here, the sensor operates close to it's detection limit for $306nm$ and $315nm$ during totality, clearly visible in the large fluctuations. The ratio at $306nm$ is not plotted therefore. Outside the totality, all wavelengths are simulated too low. If this would be attributable to ozone, one would expect a systematic deviation towards shorter wavelengths, which is not the case. $340nm$ shows very good agreement, whereas $380nm$ and $395nm$ have the strongest deviation. Because the simulation agrees much better to the measurements at $412nm$, this seems especially remarkable. In contrast to the $306nm$ and $315nm$ channels, which are calibrated against a spectroradiometer from the US National Science Foundation's Ultraviolet Spectral Irradiance Monitoring Network, the other wavelengths were all subject to the same calibration process. A possible contribution to the difference between $395nm$ and $412nm$ might be uncertainties in the limb darkening parametrizations, e.g. Neckel provides no data between $373nm$ and $385nm$ as a consequence of the Balmer jump in this region. However, the difference between Neckel's and Pierce' parametrization is not huge enough at $395nm$ and $412nm$ to attribute this jump solely to uncertainties in the limb darkening (compare Figure 4.17a).

In Figure 4.17a, the temporal averaged ratios during the first $10s$ of totality are shown. It reflects most of the features already discussed above. The errorbars point out the standard deviation, calculated as the square root of the squared deviation from the mean (i.e. in the limit of many samples, one would expect 2/3 of them in the given intervals). They get important for example at $315nm$ and $940nm$, agreeing only on average within 1% with the measurements. Simulations were made with Neckel's and Pierce' limb darkening parametrization. The influence of the parametrization is strongest in the $400nm$ - $600nm$ domain, with the difference between the ratios peaking at $395nm$ with Neckel's simulation results lowered by 4%. This is also indicated by Figure 3.7b, where $412nm$ shows higher intensities in Pierce' than in Neckel's parametrization. Nevertheless, it was not possible to find a direct correlation over all wavelengths between the deviations of the parametrizations in Figure 3.7b and the differences in Figure 4.17a. With the differences in the simulation resulting from the limb darkening parametrizations being approximately one order of magnitude smaller than the actual differences between simulation and measurements, it would be hard to make predictions about the correctnes of one or the other of the two parametrizations anyway.

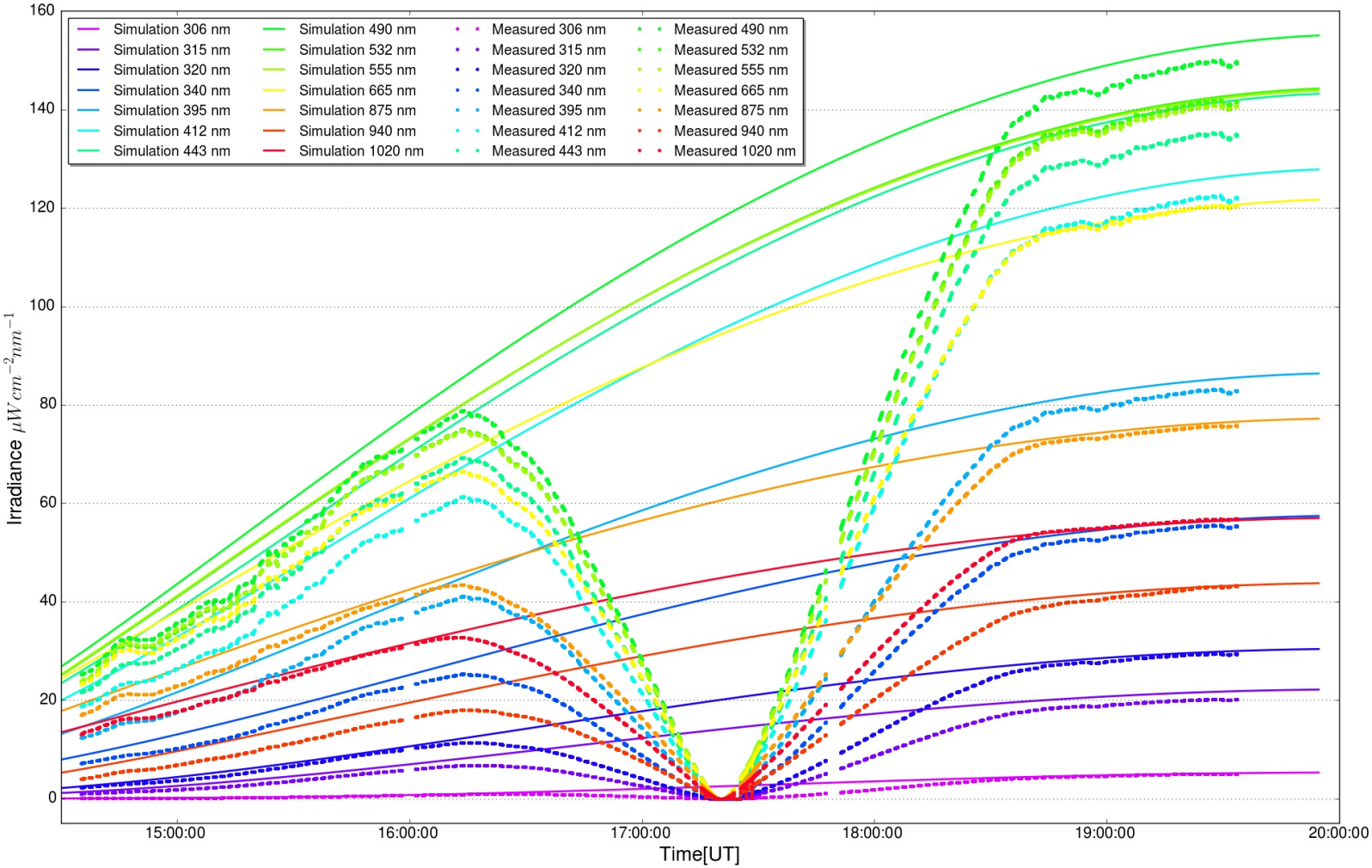

Figure 4.12: Simulated irradiance for non-eclipse conditions together with measurements, covering the whole time of the eclipse 2017.

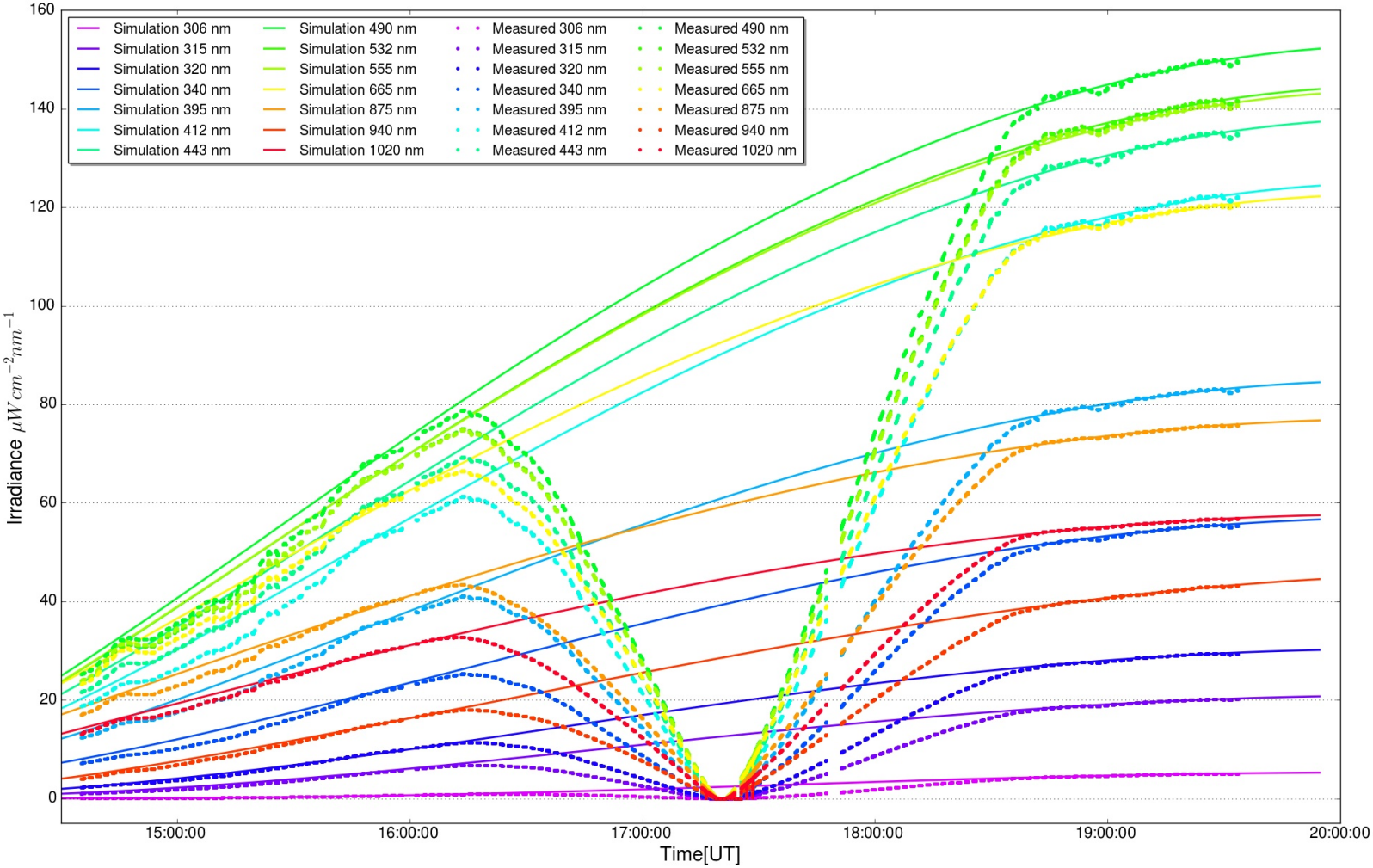

Figure 4.13: Simulated irradiance for non-eclipse conditions together with measurements, covering the whole time of the eclipse 2017. The simulation was multiplied with a correction factor to fit the measured values after 19:00 UT.

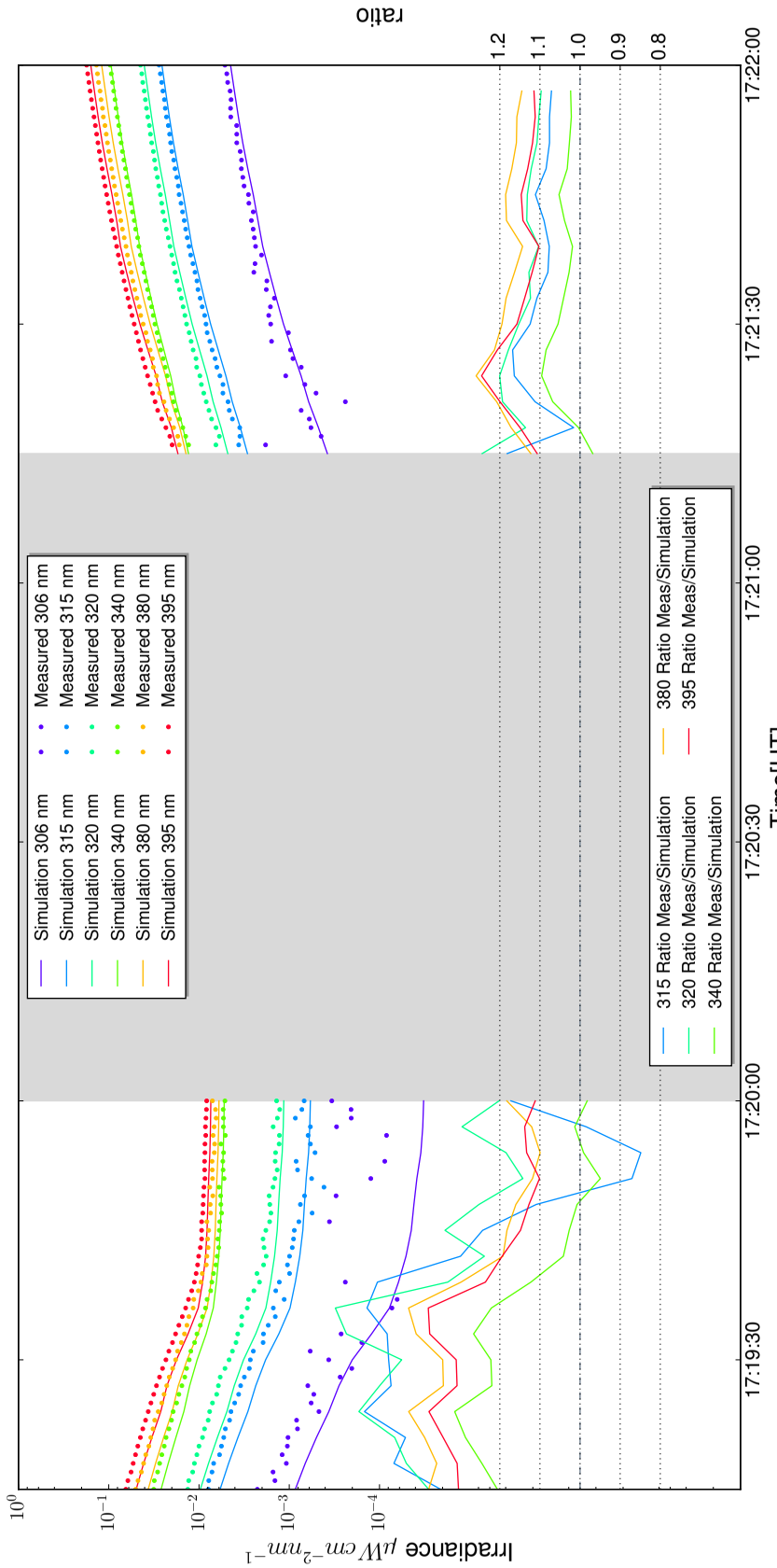

Figure 4.14: Simulated and measured irradiance for wavelengths from $300nm$ to $400nm$. The grey area indicates times of shadowbanding.

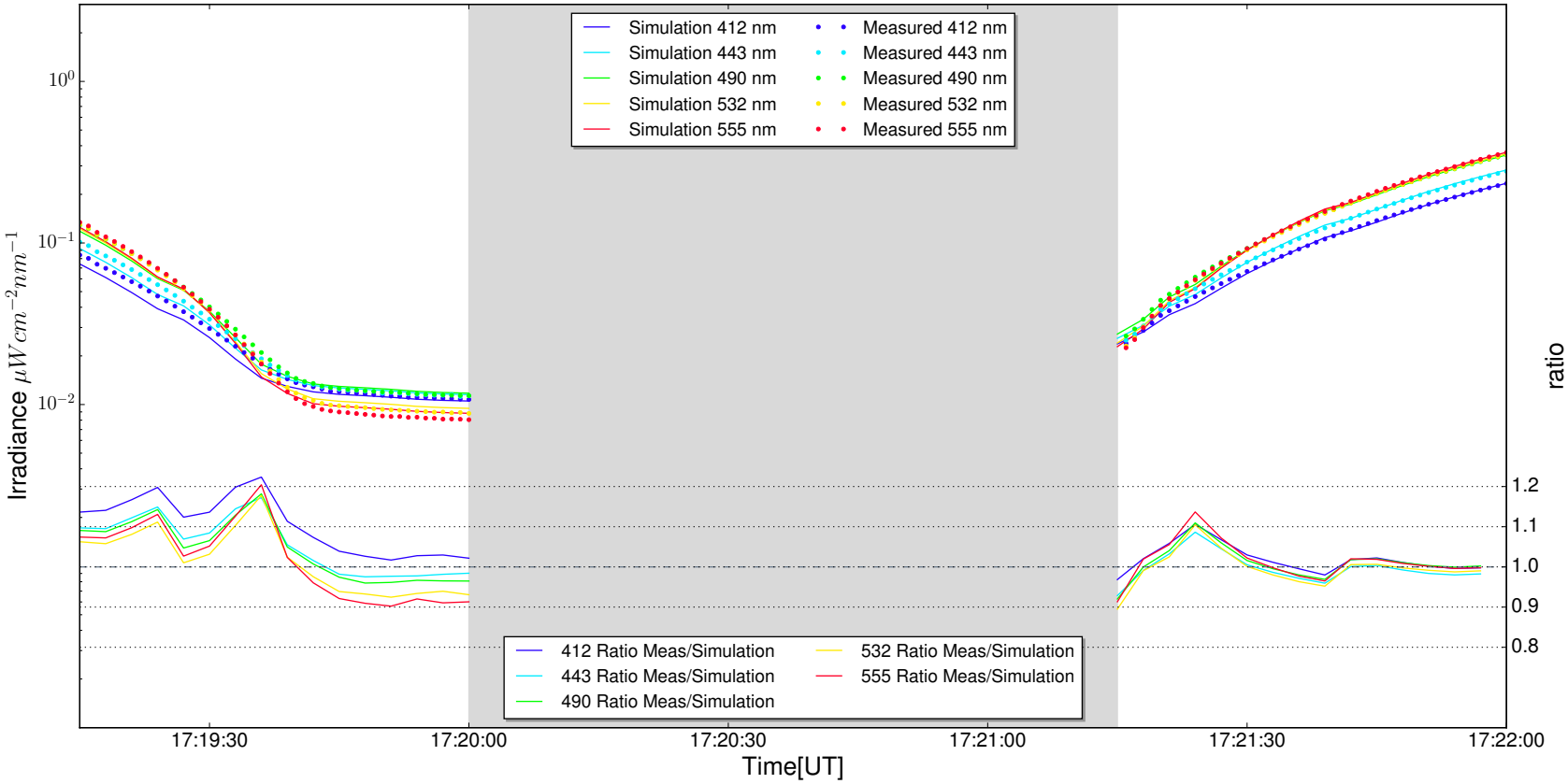

Figure 4.15: Simulated and measured irradiance for wavelengths from $400nm$ to $600nm$. The grey area indicates times of shadowbanding.

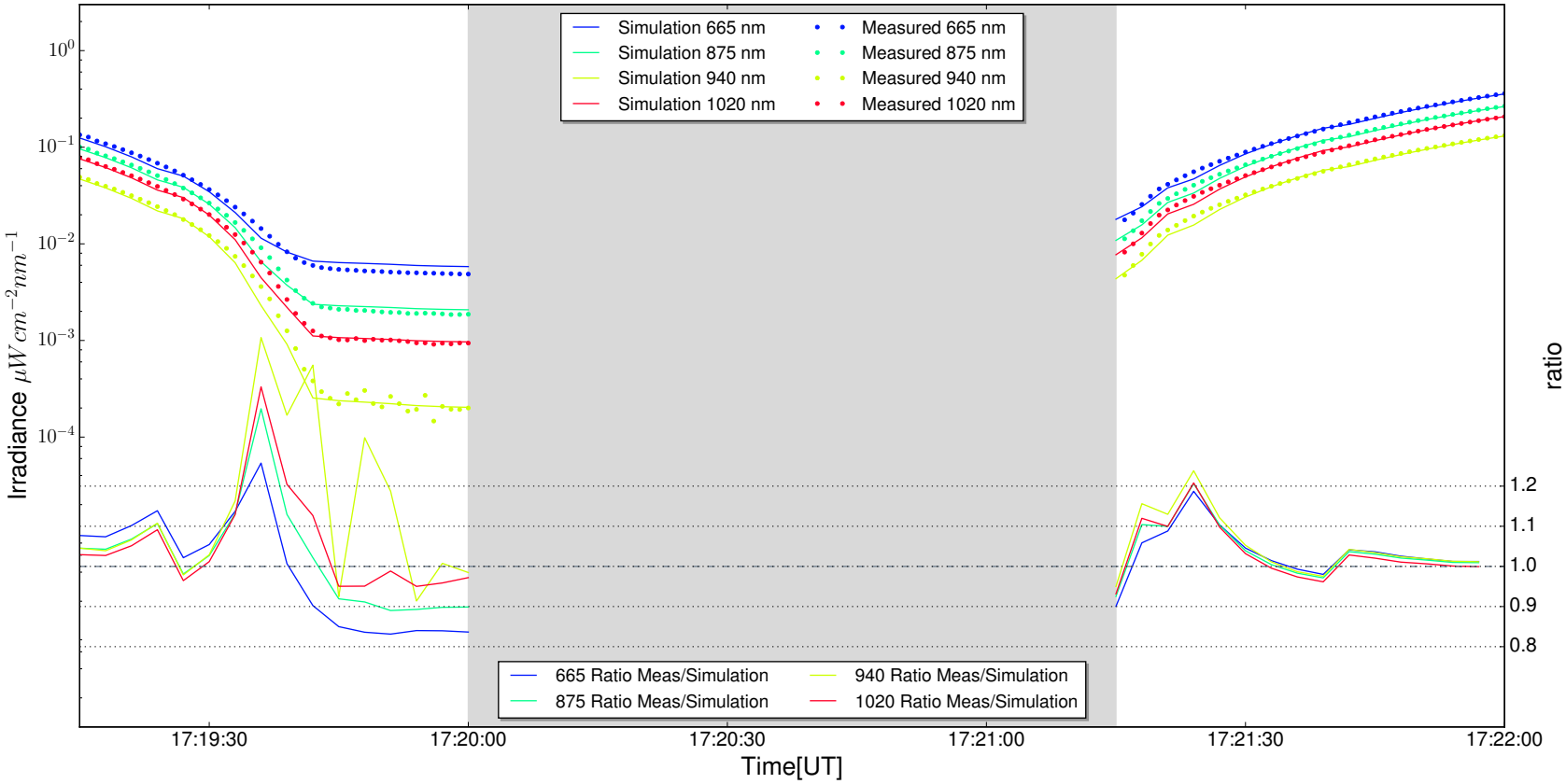

Figure 4.16: Simulated and measured irradiance for wavelengths from 600nm to 1020nm. The grey area indicates times of shadowbanding.

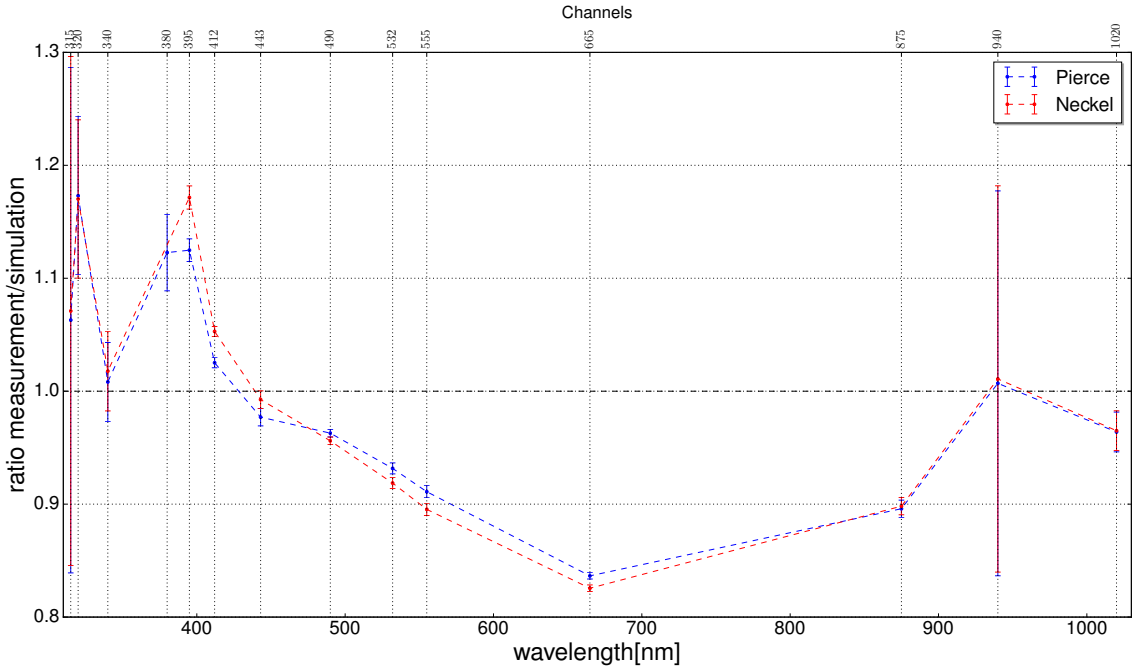

(a) Averaged ratio of measurement and simulation for the beginning of the totality (17:19:48UT - 17:20:00UT). The errorbars indicate 1σ-deviation of the original values from the mean. Simulations were performed with Neckel's and Pierce' solar limb darkening parametrization.

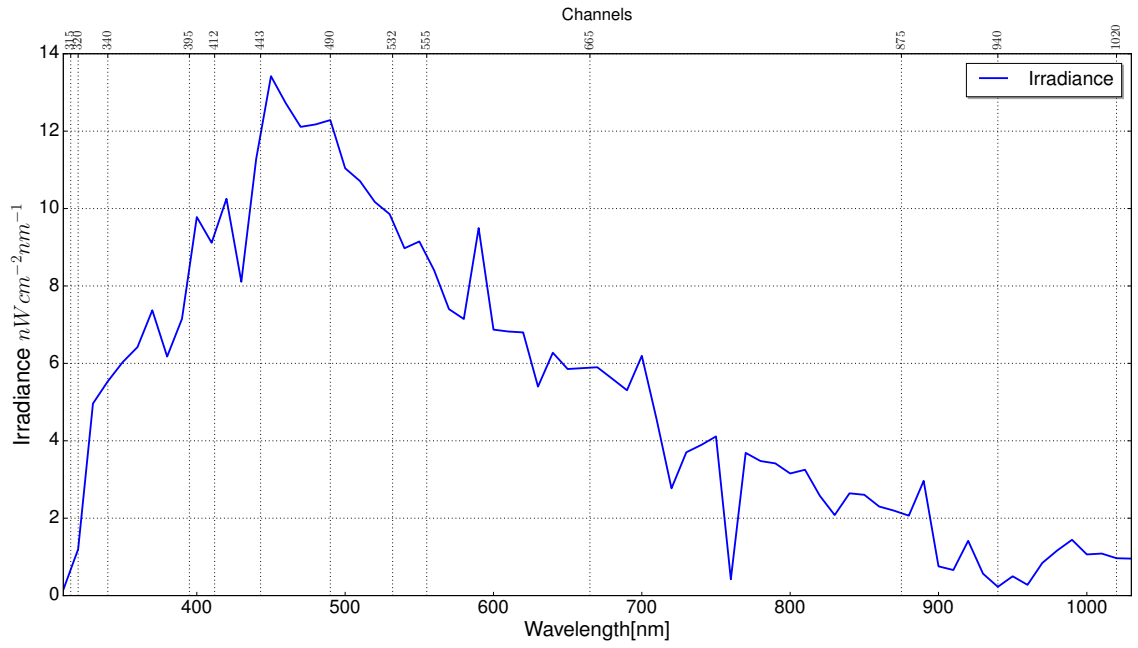

(b) Simulated irradiance for wavelengths between $310nm$ and $1020nm$ at 17:20UT. Note that irradiance is given in $nWcm^{-2}nm^{-1}$.

Figure 4.17

Chapter 5

The total solar eclipse 2019

To prove the model's ability to simulate different eclipses, the total solar eclipse on July 02, 2019 will be simulated in this chapter. The eclipse will take place in the southern hemisphere mainly over the pacific ocean, before reaching the western coast of South America in the evening and traversing over Chile and Argentinia. The full path is shown in Figure 5.1a. With an apparent moon to sun ratio of 1.039 and 130km diameter of the umbral shadow when reaching the coast, the eclipse is a little more intense than the one 2017 in Smith Rock State Park. What makes this eclipse really special is the unique chance for observations: The La Silla Observatory, operated by the European Southern Observatory (ESO), is located 50km from the umbral shadow's center line and covered by the umbral shadow for nearly two minutes. The eclipse times at the observatory (29°14'45"S 70°44'13"W) are given in Table 5.1. Situated in a height of 2400m at the edge of the Atacama Desert, there is only minimal light pollution. Typical weather conditions are plotted in Figure 5.2. Although June and July show the worst conditions in the annual cycle, the chance for nights where at least spectroscopic measurements are possible is still around 70% to 80%. Besides the good environmental conditions, the possibility to use astronomical devices to measue radiative quantities could lead to precise results even in the ultraviolet domain due to the high sensitivity of the telescopes. In fact, some kind of filter has to be installed very likely to protect the sensors. The eclipse taking place in the late afternoon (Chile's time zone is UT-4), turns out to be an advantage from this point of view.

Simulations were done with a standard atmospheric setup, similar to the first approach in section 4.2: No aerosol was specified and albedo is kept spectrally constant to 0.05. The midlatitude summer profile is used, interpolated to a height of 2400m a.s.l. and with Ozone set to 298DU. Pierce' limb darkening parametrization is applied. Curves for the temporal change of irradiance can be seen in Figure 5.3a. Comparing them to Figure 4.2, the overall pattern is the same, with drops in irradiance by three to four orders of magnitude within 10min before and after totality. The absolute intensities during totality are lower by approximately one order of magnitude. Looking at the shape of the curves, the deformation already discussed for the eclipse 2017 is clearly visible, but in the opposite way. This is conform with the conditions 2019: With the sun located in the north-west and the shadow traveling from west to east, the direct radiation is now suppressed before the observer-sun line rather than after. Since the sun is standing close to the horizon, this effect turns out to be significant. For the UV wavelengths, there is almost no direct radiation at these times, so they don't jump up at the end of the totality, but increase more slowly towards their clearsky value. The spectrum of irradiance at 20:40:20UT can be seen in Figure 5.3b.

Event	Time[UT]	Elevation[°]	Azimuth[°]
Start partial eclipse	19:23:50.3	25.5	319.9
Start total eclipse	20:39:23.7	13.5	306.5
Maximum eclipse	20:40:19.5	13.3	306.4
End total eclipse	20:41:15.0	13.2	306.2
End partial eclipse	21:47:16.4	00.9	297.2

Table 5.1: Times and solar angle for different characteristic events of the eclipse 2019 at La Silla Observatory. Elevation is given relative to the horizon, azimuth is measured clockwise from the north (JPL convention). Created with Espenak 2018.

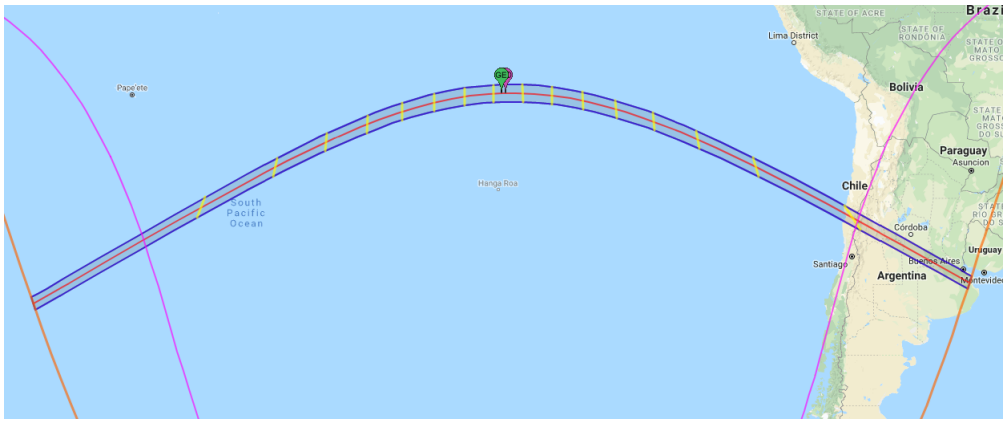

(a)

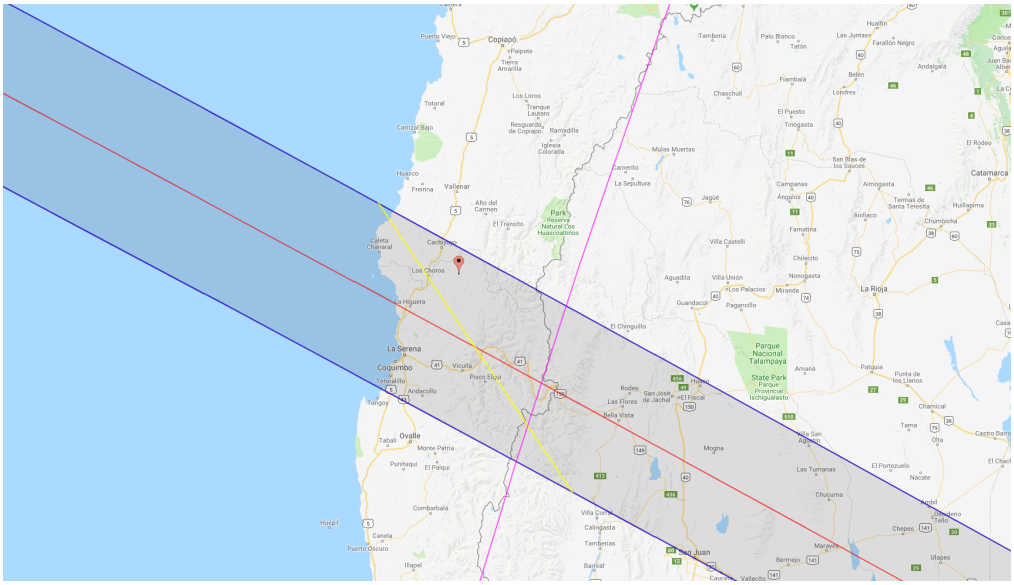

(b)

Figure 5.1: Path of the umbral shadow on July 02, 2019 over the pacific ocean in Figure 5.1a and over the Chilean coast in Figure 5.1b. The red marker shows the position of the La Silla observatory, green and magenta markers show the place of greatest eclipse and longest totality time. Produced with Espenak 2018.

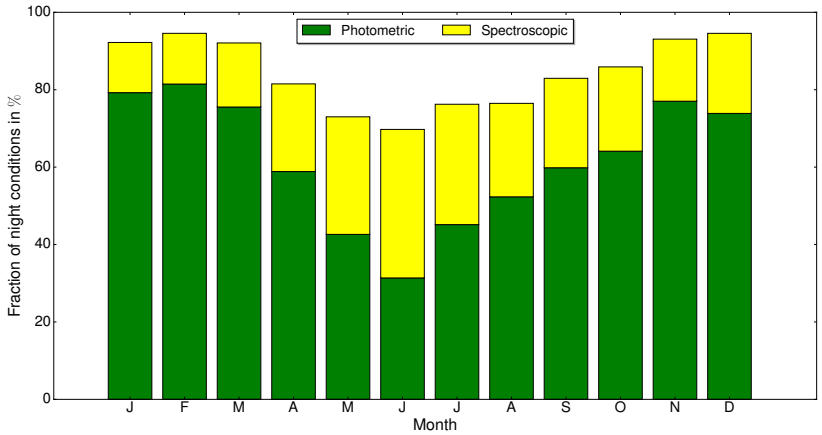

Figure 5.2: Percentage of nights at La Silla observatory, where photometric and spectroscopic conditions are fulfilled. Photometric conditions are defined by ESO as nights showing no visible clouds and transparency variations under 2%. The data was averaged from the years 1991 until 1999, taken from *La Silla Weather Information* 2018.

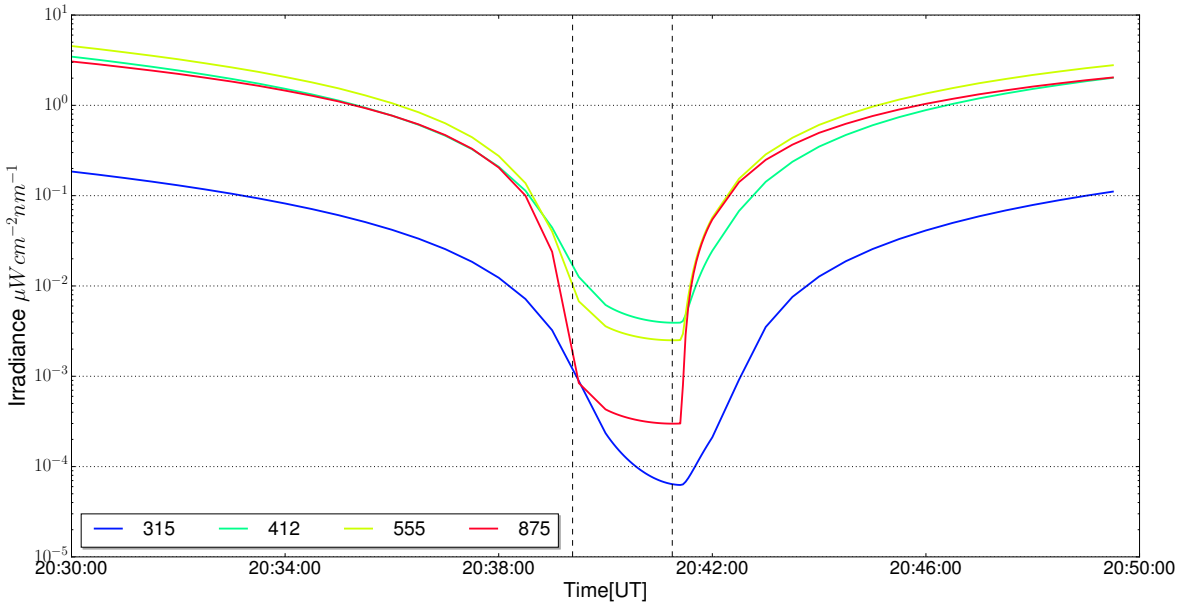

(a)

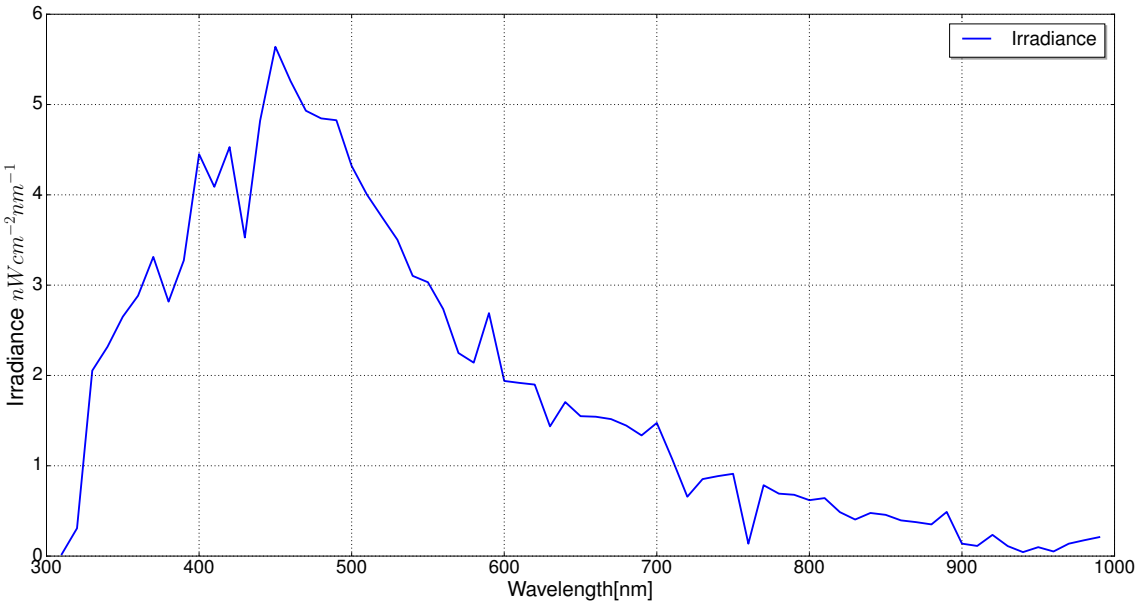

(b) Spectal distribution of solar irradiance at time of maximum totality (20:40:20UT). Simulation in steps of $10nm$. Note that irradiance in given in $nWcm^{-2}nm^{-1}$.

Figure 5.3

Chapter 6

Conclusion and Outlook

In this work, a three-dimensional model to simulate atmospheric radiative transfer during an eclipse was set up. The celestial part includes precise trajectories of the sun and moon, as well as parametrizations for the limb darkening of the sun. The atmosphere contains realistic gas profiles, a surface with spectral dependent reflection and a simple topography model. The simulation was applied to the total solar eclipses 2017 and 2019, and the influence of the surface, ozone and the topography were examined. Subsequently, the simulations were compared with measurements taken 2017. It is shown that solar irradiance during the course of the eclipse can be modeled with high accuracy, showing less than 20% deviation during the totality. Considering the huge influence of the suface albedo and mountain profile, creating changes up to 200%, the agreement between measurement and simulation is as close as one could hope for.

Nevertheless, some of the settings show potential for further improvement. For a realistic simulation of the environment, the surface albedo would have to be a two-dimensional, wavelength-dependent map. It could be obtained either directly from satellite reflectance measurements like e.g. provided by the MODIS satellite, or maybe indirectly, applying known reflectance curves for different materials to maps with information about the typical surface coverage in certain areas. In subsection 4.2.3, the possible influence of such maps was examined and a proposal for the resolution was derived. The same applies for the mountains, where a detailed elevation map of the model domain would be ideal. Furthermore, the analysis applied to ozone could be applied to other gas profiles as well. In the best case, there are not only profiles from atmospheric models available, but also sonde measurements or similar close to the observation positon and time.

With the major fraction of uncertainties therfore very likely coming from the atmospheric part, some issues in the celestial calculations still remain. For example the results are corrected for the annual variations in the sun-earth distance, but not for temporal variations in the solar activity. This can play a small role in the ultraviolet, where 2017 measurements show much noise anyway, but could maybe be worth considering for future measurements with astronomical equipment. Some technical points also show potential for improvement. With the current solution, the programm offers maximal flexibility to read in files with astronomical data. However, there are some libraries like e.g. by Rhodes 2018 available, allowing to create the celestial data within the simulation itself, supposed they provide accuracy comparable to the JPL Horizons algorithms.

The simulations for the eclipse 2019 form the basis for planning future measurements. Depending on the devices that will be used, it could be necesary to simulate radiance rather than irradiance. This can be easily done by specifying *umu* and *phi* in the MYSTIC input, defining the viewing direction of the sensor. The rest of the simulation process stays the same. With the option *mc_polarization*, it is possible to simulate polarized radiative transfer. Applying some small changes in the output processing, the programm already has been proven the ability to do so. This opens a completely new field of study, certainly hiding some interesting features. The results still need further investigation and will be published in future.

Acknowledgements

I would first like to thank Dr. Claudia Emde and Prof. Dr. Bernhard Mayer who supervised this study. They were always available for questions and provided many helpful tips in order to create my first longer, scientific work. Furthermore, thanks go to Germar Bernhard, who carried out the measurements 2017 and accompanied the complete thesis with suggestions and answers to my question-filled emails. Thank you!

Appendices

Appendix A

Overview of coordinate systems

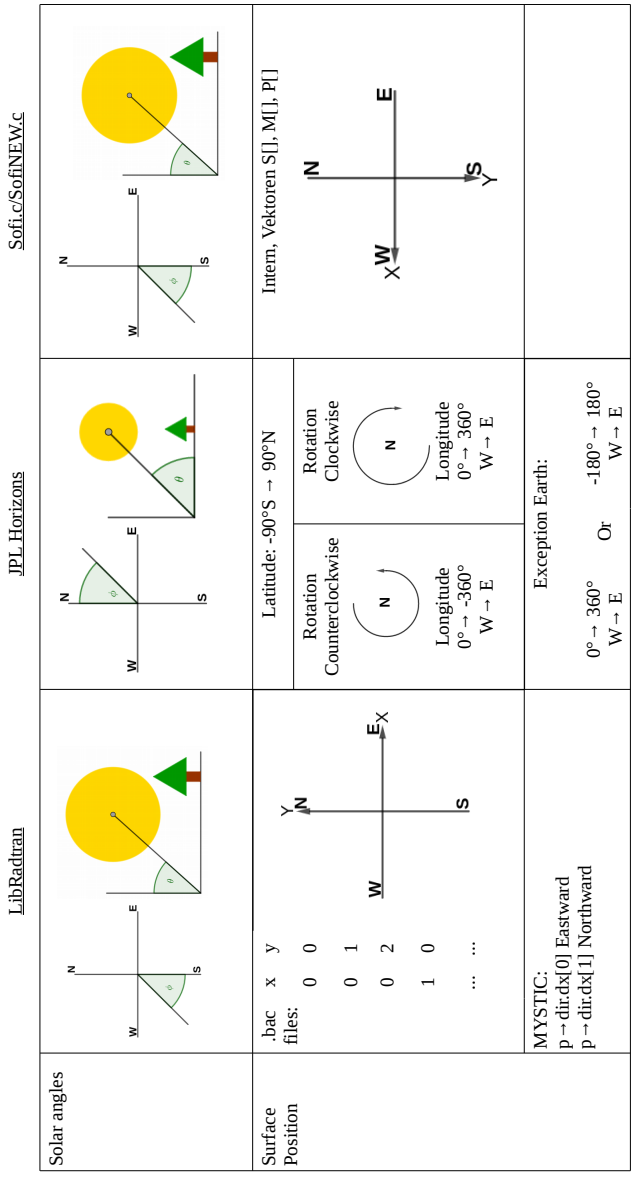

Figure A.1

Appendix B

Measurements with Shadowband

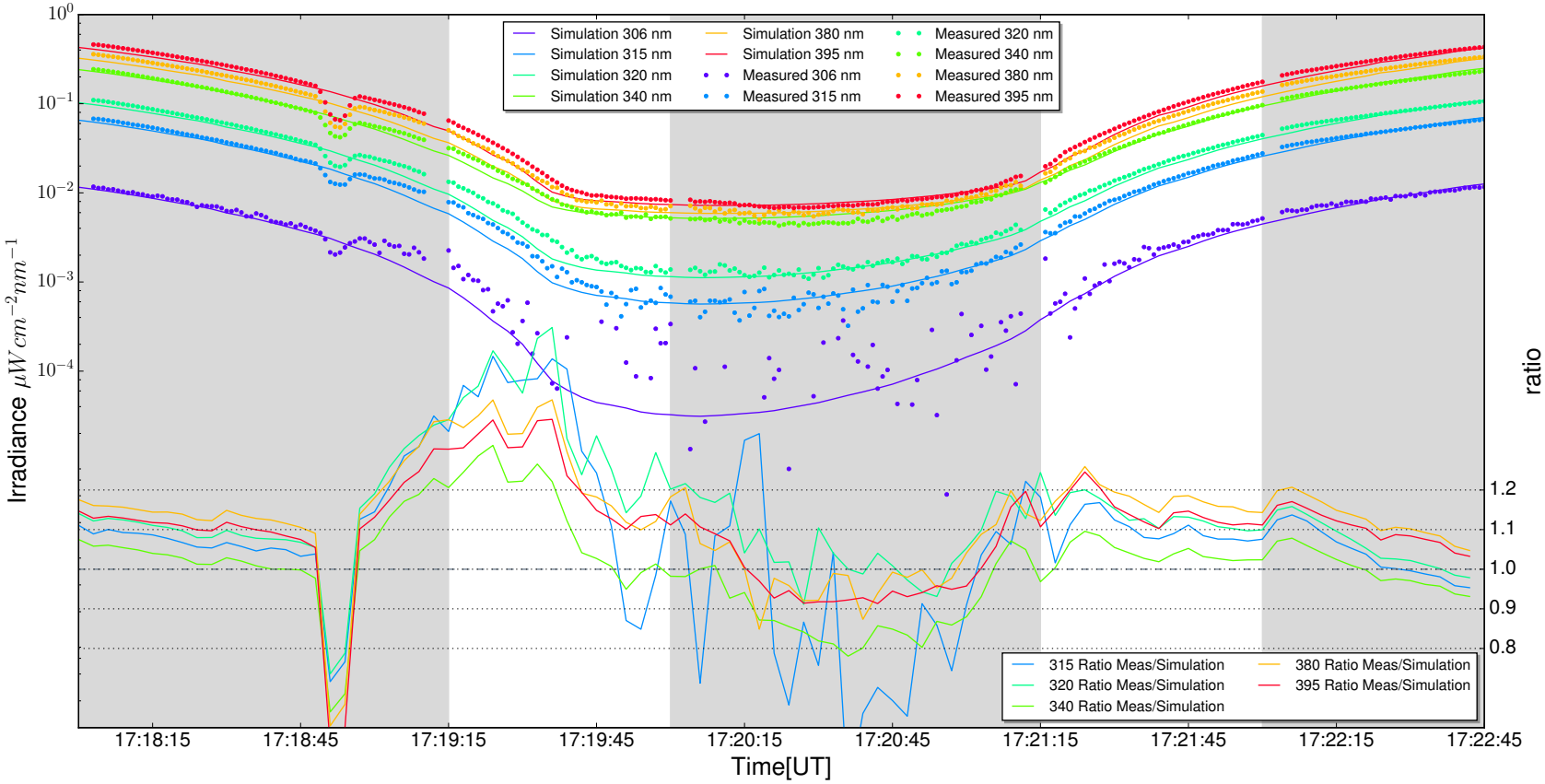

Figure B.1: Simulated and measured irradiance for wavelengths from 300nm to 400nm. Grey shaded areas indicate times with shadowband influence.

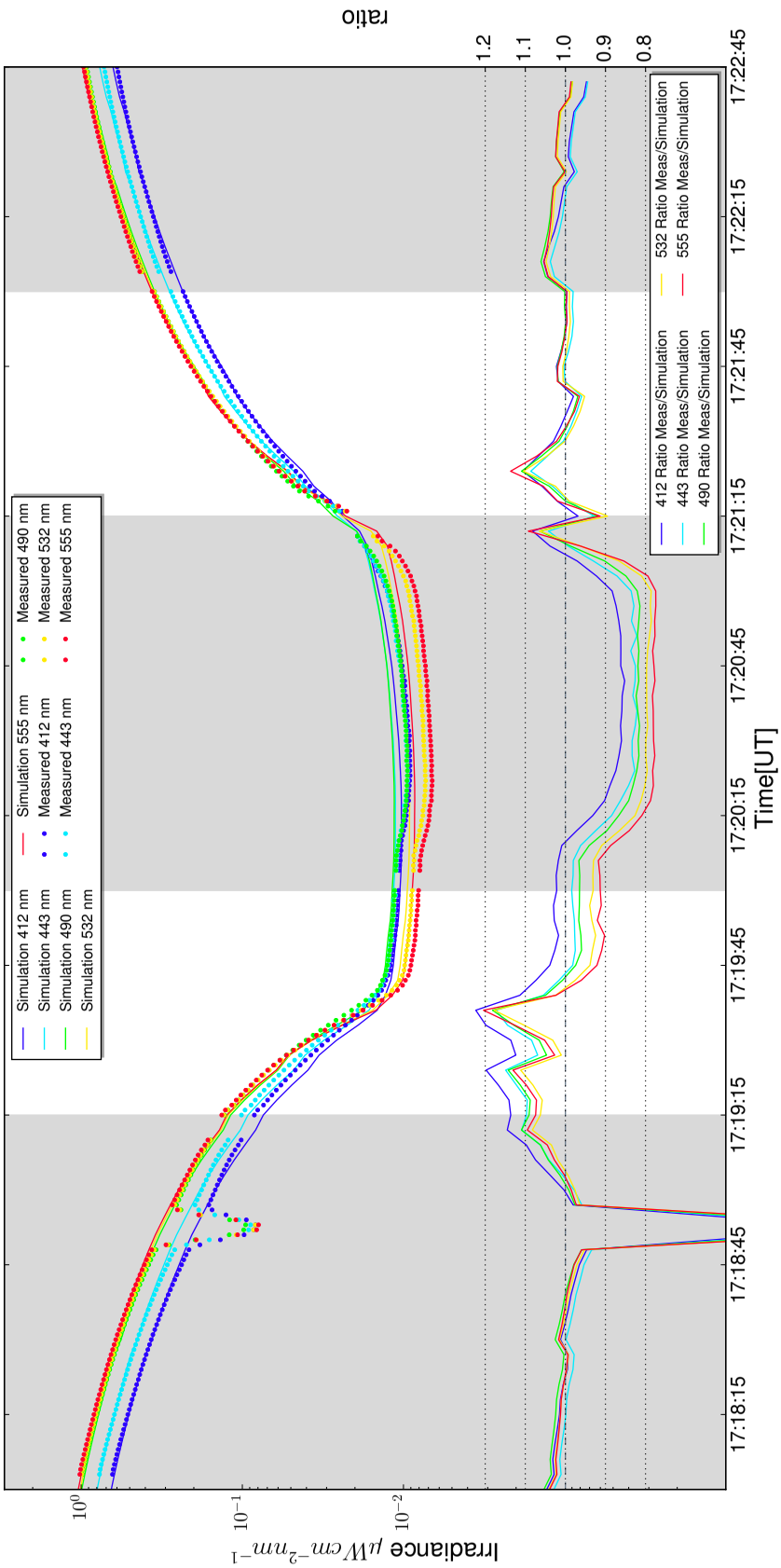

Figure B.2: Simulated and measured irradiance for wavelengths from $400nm$ to $600nm$. Grey shaded areas indicate times with shadowband influence.

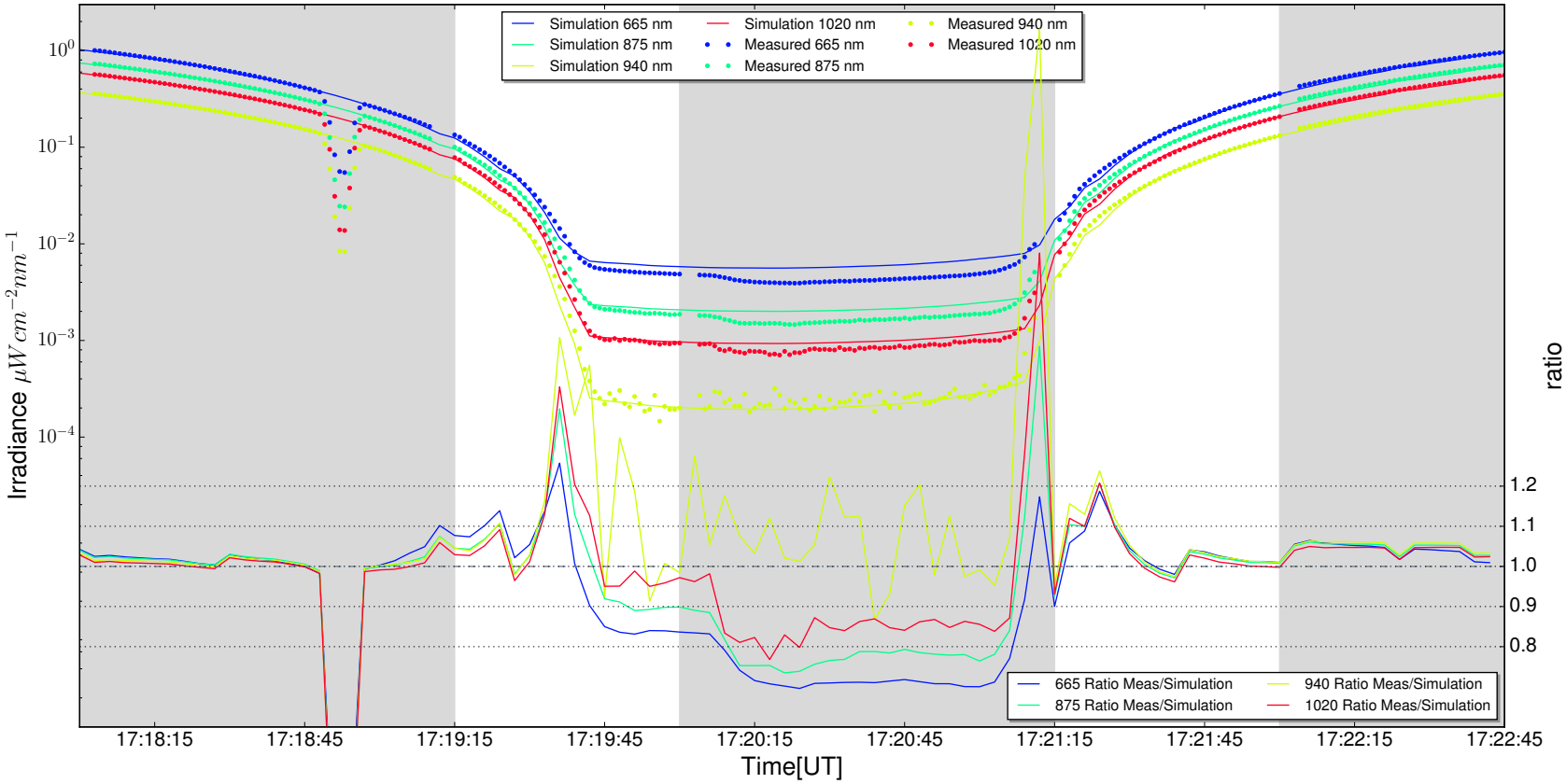

Figure B.3: Simulated and measured irradiance for wavelengths from 600nm to 1020nm. Grey shaded areas indicate times with shadowband influence.

Bibliography

Anderson, G. et al. (1986). *AFGL Atmospheric Constituent Profiles(0-120km)*. Hanscom AFB, MA 01731: Air Force Geophysics Laboratory.

Bernhard, G., C. Booth, and J. Ehramjian (2004). "Version 2 data of the National Science Foundation's Ultraviolet Radiation Monitoring Network". In: *Solar Energy* 74 (4), pp. 423–453.

Bernhard, G. and B. Mayer (2018). "Measurements of spectral irradiance during the solar eclipse of 21 August 2016: solar limb darkening, changes in total ozone. (in preparation)".

Buras, R., T. Dowling, and C. Emde (2011). "New secondary-scattering correction in DISORT with increased efficiency for forward scattering". In: *Journal of Quantitative Spectroscopy and Radiative Transfer* 112.12, pp. 2028–2034. ISSN: 0022-4073. DOI: https://doi.org/10.1016/j.jqsrt.2011.03.019. URL: http://www.sciencedirect.com/science/article/pii/S0022407311001385.

Dee, D. P. et al. (2011). "The ERAInterim reanalysis: configuration and performance of the data assimilation system". In: *Quarterly Journal of the Royal Meteorological Society* 137.656, pp. 553–597. DOI: 10.1002/qj.828. eprint: https://rmets.onlinelibrary.wiley.com/doi/pdf/10.1002/qj.828. URL: https://rmets.onlinelibrary.wiley.com/doi/abs/10.1002/qj.828.

Demtröder, W. (2016). *Experimentalphysik 3. Atome,Moleküle und Festkörper*. Berlin, Heidelberg: Springer. ISBN: 978-3-662-49093-8.

ECOSTRESS spectral library (2018). Jet Propulsion Laboratory, California Institue of Technology. URL: https://speclib.jpl.nasa.gov/library (visited on 05/10/2018).

Emde, C., R. Buras-Schnell, et al. (2016). "The libRadtran software package for radiative transfer calculations (version 2.0.1)". In: *Geoscientific Model Development* 9.5, pp. 1647–1672. DOI: 10.5194/gmd-9-1647-2016. URL: https://www.geosci-model-dev.net/9/1647/2016/.

Emde, C. and B. Mayer (2007). "Simulation of solar radiation during a total eclipse: a challenge for radiative transfer". In: *Atmospheric Chemistry and Physics* 7, pp. 2259–2270. URL: https://www.atmos-chem-phys.net/7/2259/2007/ (visited on 04/30/2018).

Emmons, L. K. et al. (2010). "Description and evaluation of the Model for Ozone and Related chemical Tracers, version 4 (MOZART-4)". In: *Geoscientific Model Development* 3.1, pp. 43–67. DOI: 10.5194/gmd-3-43-2010. URL: https://www.geosci-model-dev.net/3/43/2010/.

Espenak, F. (2018). *EclipseWise.com*. URL: http://www.eclipsewise.com/solar/SEgmap/2001-2100/SE2017Aug21Tgmap.html.

Espenak, F. and J. Anderson (2004). *Total solar eclipse of 2006 March 29*. Goddard Space Flight Center.

Gasteiger, J. et al. (2014). "Representative wavelengths absorption parameterization applied to satellite channels and spectral bands". In: *Journal of quantitative Spectroscopy and Radiative Transfer* 148, pp. 99–115.

Google Maps (2018). URL: https://www.google.com/maps.

Gueymard, C. (2004). "The sun's total and spectral irradiance for solar energy applications and solar radiation models". In: *Journal of Geophysical Research* 109. DOI: 10.1029/2004JD004937.

Iqbal, M. (1983). *An Introduction to Solar Radiation*. Don Mills, Ontario, Canada: Academic Press. ISBN: 0-12-373750-8.

JPL Horizons On-Line Ephemeris System (2018). Jet Propulsion Laboratory, California Institue of Technology. URL: https://ssd.jpl.nasa.gov/?horizons_doc (visited on 04/21/2018).

Koepke, P., J. Reuder, and J. Schween (2001). "Spectral variation of the solar radiation during an eclipse". In: *Meteorologische Zeitschrift* 10.3, pp. 179–186.

Synthetic infrared spectra (1992). IAU Symp. 154. Norwell, MA.

La Silla Weather Information (2018). European Southern Observatory. URL: https://www.eso.org/sci/facilities/lasilla/astclim/weather.html (visited on 05/28/2018).

Marshak, A. and A. Davis (2005). *3D Radiative Transfer in Cloudy Atmospheres*. Berlin,Heidelberg: Springer-Verlag. ISBN: 3-540-23958-8.

Mayer, B. and A. Kylling (2005). "Technical note: The libRadtran software package for radiative transfer calculations - description and examples of use". In: *Atmospheric Chemistry and Physics* 5.7, pp. 1855–1877. DOI: 10.5194/acp-5-1855-2005. URL: https://www.atmos-chem-phys.net/5/1855/2005/.

Mayer, B. (2009). "Radiative transfer in the cloudy atmosphere". In: *European Physical Journal Conferences* 1, pp. 75–99.

Minnaert, M. (1953). *The sun*. Chicago: The University of Chicago Press, p. 88.

NASA Earth Fact Sheet (2018). NASA Goddard Space Flight Center. URL: https://nssdc.gsfc.nasa.gov/planetary/factsheet/earthfact.html (visited on 05/01/2018).

NASA Moon Fact Sheet (2018). NASA Goddard Space Flight Center. URL: https://nssdc.gsfc.nasa.gov/planetary/factsheet/moonfact.html (visited on 05/01/2018).

NASA World View (2018). NASA EOSDIS (Earth Observing System Data and Information System). URL: https://worldview.earthdata.nasa.gov/ (visited on 05/15/2018).

Neckel, H. (2005). "Analytical reference functions F(λ) for the fun's limb darkening and its absolute continuum intensities". In: *Solar Physics* 229, pp. 13–33.

Neckel, H. and D. Labs (1994). "Solar limb darkening 1986-1990". In: *Solar Physics* 153, pp. 91–114.

Pierce, A. K. and C. D. Slaughter (1977). "Solar limb darkening". In: *Solar Physics* 51, pp. 25–41.

Pierce, A. K., C. D. Slaughter, and D. Weinberger (1977). "Solar limb darkening". In: *Solar Physics* 52, pp. 179–189.

Rhodes, B. (2018). *PyEphem*. Version 3.7.6.0. URL: http://rhodesmill.org/pyephem/index.html.

Stamnes, K. et al. (1988). "Numerically stable algorithm for discrete-ordinate-method radiative transfer in multiple scattering andemitting layered media". In: *Applied Optics* 27.12.

U.S. Geological Survey Spectral library (2018). URL: https://speclab.cr.usgs.gov/spectral.lib04/spectral-lib04.html (visited on 05/10/2018).

Waldmeier, M. (1955). *Ergebnisse und Probleme der Sonnenforschung*. Vol. 2. Akademische Verlagsgesellschaft Geest&Portig K.G.

Young, A. (2018). *NASA eclipse website*. Heliophysics Science Division, Code 670 NASA Goddard Space Flight Center. URL: https://eclipse.gsfc.nasa.gov/eclipse.html (visited on 04/21/2018).

Zdunkowski, W., T. Trautmann, and A. Bott (2007). *Radiation in the Atmosphere. A Course in Theoretical Meteorology*. Cambridge: Cambridge University Press. ISBN: 978-0-521-87107-5.

Hiermit erkläre ich, die vorliegende Arbeit

Simulation der solaren Bestrahlungsstärke während einer totalen Sonnenfinsternis

selbständig verfasst zu haben und keine anderen als die in der Arbeit angegebenen Quellen und Hilfsmittel benutzt zu haben.

Ort,Datum Unterschrift